Tuning miscibility and morphology at the nanoscale: First-principles investigations

A Thesis

Submitted For the Degree of

MASTER OF SCIENCE

in the Faculty of Science

by

Nisha Mariam Mammen

CHEMISTRY AND PHYSICS OF MATERIALS UNIT
JAWAHARLAL NEHRU CENTRE FOR ADVANCED SCIENTIFIC RESEARCH
Bangalore – 560 064

AUGUST 2010

To my parents

DECLARATION

I hereby declare that the matter embodied in the thesis entitled "**Tuning miscibility and morphology at the nanoscale: First-principles investigations**" is the result of investigations carried out by me at the Chemistry and Physics of Materials Unit, Jawaharlal Nehru Centre for Advanced Scientific Research, Bangalore, India under the supervision of Prof. Shobhana Narasimhan and that it has not been submitted elsewhere for the award of any degree or diploma.

In keeping with the general practice in reporting scientific observations, due acknowledgement has been made whenever the work described is based on the findings of other investigators.

Nisha Mariam Mammen

CERTIFICATE

I hereby certify that the matter embodied in this thesis entitled "**Tuning miscibility and morphology at the nanoscale: First-principles investigations**" has been carried out by Ms. Nisha Mariam Mammen at the Chemistry and Physics of Materials Unit, Jawaharlal Nehru Centre for Advanced Scientific Research, Bangalore, India under my supervision and that it has not been submitted elsewhere for the award of any degree or diploma.

Prof. Shobhana Narasimhan
(Research Supervisor)

Acknowledgements

My deepest gratitude to my advisor, Prof. Shobhana Narasimhan for giving me the opportunity to work with her and for creating a wonderful research environment in the group. She introduced me to the field of solid state physics, computational nanoscience, and to many interesting problems I could work on. She gave me the opportunity to visit Trieste, (SISSA and ICTP) and interact with many scientists and understand their style of research. Her positive outlook, unmatched patience and zeal has been a great source of inspiration. I'm grateful to her for setting high bench marks and high standards, and motivating me to achieve them. I also wish to thank her for patiently correcting and forgiving my flaws and being there for me when I was going through low times in my life.

I cordially thank our collaborator on the Au clusters project, Prof. Stefano de Gironcoli. His patience in answering questions, approach to problems and passion for physics has inspired me to pursue a career in the field of theoretical science.

I would like to thank Prof. C.N.R. Rao and Prof. M. R. S. Rao for providing excellent research facilities, creating a scientific environment in JNCASR and teaching us to be leaders in science.

I sincerely thank the coordinators of the Integrated PhD Program, Prof. G. U. Kulkarni and Prof. S. Balasubramanian for giving me the opportunity to be part of this institute and for their constant encouragement and support.

I thank Prof. S. Ranganathan, Prof. Chandrabhas Narayana, Prof. Umesh Waghmare, Prof. Swapan K. Pati, Prof. S.M. Shivaprasad, Prof. K. S. Narayan, Prof. A. Sundaresan, Dr. Vidhyadhiraja, Dr. Tapas Maji, Dr. M. Eswarmoorthy, Dr. Subi George, and Dr. T. Govindraju for the courses they offered and for guiding me to think in a scientific manner. I acknowledge many faculty in JNCASR, with whom I have had the opportunity to interact on matters of science and otherwise. I wish to thank all my teachers and everyone who has helped shape my interest in science. I remember especially, Dr. Sunitha Rani who taught me in 7th grade and ignited in me the love for chemistry.

I thank all the academic staff, administrative staff, library staff, complab staff and hostel staff for providing and helping me with the facilities in JNC.

I wish to thank all my lab mates, Mighfar Imam, Madhura Marathe, Kanchan Ulman and Sananda Biswas for their support and care, for being patient with me and bearing the noisy person that I am. My gratitude to all TSU members for fruitful discussions on physics. All my batch mates and friends in JNC, I thank them for making the course work and hostel life enjoyable and memorable.

I also thank my parents and sister for always being there for me and for their constant encouragement and support to pursue my interest in science.

Thank you Lord!

Synopsis

This thesis is divided into five chapters.

(A)The first chapter in the thesis gives a brief introduction and motivation for studying low dimensional systems. We have discussed about how the properties change very drastically when going from bulk to a lower dimensional scale. The importance of theoretical calculations and how it can help in the study of such materials are discussed. Computational science can help suggest new materials with desired properties, and can also help understand and explain experimental results by analysing the factors involved separately. The theoretical tools used for the calculations in the work reported in this thesis are briefly mentioned.

(B)The second chapter of the thesis gives a brief description on density functional theory (DFT). An introduction to the many-body problem and the approximations involved are discussed. The techniques used for implementing the density functional theory like plane-wave basis set, k-point sampling and smearing are explained. The theory of calculating forces on the atoms by the Hellmann-Feynman theorem is discussed. The framework of spin-polarised DFT used for the calculation of magnetic properties of systems is also briefly described.

(C) The third chapter is dedicated to the study of "Surface alloys on a W(110) substrate". It deals with two-dimensional systems of surface alloys, obtained by mixing two different metals over the surface of another metal. Metals that do not form alloys in the bulk phase may allow an atomic level mixing at the surface. Surface alloys become even more interesting when at least one of the constituents is magnetic, as both lower coordination at the surface and the change in effective coordination number due to alloying can have significant impact on the magnetic properties of the system.

We chose eight different metals, three magnetic and five non-magnetic metals, belonging to a range of sizes and studied the surface alloy formation over the W(110). We studied the properties of the single-component monolayers of these metals over W(110). We calculated preferred surface sizes of the atoms on the W(110) surface using stress calculations. We also investigated the stability and the magnetic property of the alloys formed (four configurations of alloys considered for every pair of magnetic and non-magnetic metals considered by us). We have tried to analyse the stability of these surface alloys by separating the elastic and chemical contributions to the energy.

(D) The fourth chapter is devoted to the study of "Controlling morphology of Au clusters by substrate doping". We have carried out first principles investigations on the stable geometry and morphology of a 20-atom Au cluster. Au_{20} clusters are found to be catalytically active and this property is especially desirable for oxidation reactions as Au clusters were found to adsorb oxygen molecules strongly and cause an activation of the O-O bond. The Au clusters were found to be more catalytically active when they were

deposited on defect-rich MgO (F-center defects) than on MgO without any defects. This is due to the formation of slightly negatively charged Au cluster on defect-rich MgO. It was futher calculated and experimentally proven that Au clusters on Mo-supported thin film of MgO preferred a two dimensional planar geometry than the stable tetrahedral geometry of the free cluster. Here, the planar geometry was found to be more negatively charged than the tetrahedral geometry and hence, the catalytic activity of the planar cluster was predicted to be higher. In this project, we have developed a strategy to alter the tetrahedral geometry of the free cluster to the catalytically more active planar geometry by depositing the cluster over Al-doped MgO.

(E) In the fifth chapter the salient features of the findings of the thesis are summarised and some outlook for future projects are discussed.

Contents

List of Figures

List of Tables

Chapter 1

Introduction

In this thesis, we wish to present some theoretical studies on the properties of some examples of low dimensional systems. The main theme is to explore new ideas for controlling the miscibility and morphology of these low dimensional systems. The properties of such systems differ very drastically from their corresponding homogeneous bulk form. Extrapolation of the properties of the bulk systems does not always seem to describe or predict the behaviour of the same system at lower dimensions. Some of the properties of the bulk may be enhanced or diminished in the nano-regime. In some cases, novel properties seem to arise, and properties characteristic of the bulk may disappear completely when the dimensions are reduced to the nanometre scale. The study of these materials is very fundamental and interesting. The development of nanomaterials is very promising as it can lead to miniaturization of devices. The properties of the materials can be tuned or manipulated according to the need of the application. Even small changes in the sizes within the nanoscale regime can create differences in quantities such as band

gaps or surface properties. If nanoparticles can provide desired effects similar or better than the bulk material, this will also lead to lesser quantity of materials used, and will thus reduce the expense and also reduce the waste produced.

1.1 Low dimensional systems

In low dimensional systems, the properties are significantly affected by the fact that they are finite along at least one-dimension. Examples of two-dimensional systems are surfaces, thin films or monolayers. Nanotubes, nanowires and nanorods are examples of one-dimensional systems, and clusters of atoms and quantum dots are examples of zero-dimensional systems. Reduction in dimension in all these cases result in the reduction of atomic co-ordination number at the surface. Since the surface-to-volume ratio is high, this results in very different properties from the bulk. Structural or geometrical rearrangements may occur more easily depending on the environment of the system.

Some of these features are studied in this thesis. The first part deals with the two-dimensional systems of surface alloys, obtained by mixing two different metals over the surface of another metal. Metals that do not allow formation of alloys in the bulk phase may allow atomic level mixing at the surface. These calculations were done at the request of experimentalists, to suggest which choice of metals would give a stable long range ordered surface alloy, hopefully with interesting magnetic properties. The general approach to the study was to compute the stability of many systems with

different configurations. We then tried to understand the factors that govern the mixing and formation of such materials. We calculated properties like the magnetic moments, the stresses induced, and the elastic and chemical interaction contributions to the formation of the surface alloy.

The second part of the thesis involves the study of a zero-dimensional system which is a cluster of twenty gold atoms. The properties of clusters of elements or compounds are found to be drastically different from their bulk form. The high surface-to-volume ratio, and the low coordination number of the atoms on the surface, make these clusters highly reactive. The size and geometry of these clusters are very interesting to study. It is found that clusters with certain number of atoms are especially stable. The mass spectra of clusters, both metallic and non-metallic, show a pronounced intensity for certain numbers of atoms [1, 2]. These numbers are termed magic numbers. These magic numbers may have structural or electronic origin. Often the crystal structure of a large nanocluster is the same as the bulk structure of the material, with slightly contracted lattice parameters from the bulk. Intermediate size clusters show altered crystal shapes where the total energy is minimized; the exact morphology depends on the surface energies related to the specific crystal facets of the material. Still smaller clusters typically show structures that are completely different from the bulk. A general feature for small clusters is that several structural isomers are close in energy. The properties of these isomers may vary strongly with structure. For application purposes, a certain geometry may be more preferable than another and ways to control this geometry need to be developed. We have tried to come up with a simple prescription for tailoring the geometry and morphology of a

Au_{20} cluster.

1.2 Experiments and Theory

The substantial development in experimental techniques has led to many new discoveries in the last few decades. Theory is also fast developing to understand these discoveries. Theory is an effective tool not only to understand the properties of bulk and nanomaterials, but also to search for new materials and/or novel properties.

Theory can help in understanding the origin of properties in a material by disentangling the several factors that contribute to any particular property. For example, experimentally it is difficult to separate out the effect of magnetism on a system. However, theory can compute properties of the material in the presence and absence of its magnetism, that is it can study the effects of magnetism on the properties of the system by switching it on or off. Further, experimentally, a material may occur in one or very few structures, so the information to be gathered is very limited. Theoretical calculations can study a range of hypothetical structures even if they do not exist in nature, and understand the reasons for the stability of the nature-selected structures.

In the first part of this thesis on surface alloys, we have done studies on 15 systems (with four different configurations each) of a pair metals over a tungsten substrate. This would be very tedious to do experimentally. Calculations can help reduce the wastage of materials and save a lot of time of the experimentalists by suggesting the ideal system with the desired property. The second part of the thesis involving Au clusters is motivated by the idea

of designing a novel method to control the morphology of the cluster. We wish to suggest to experimentalists this method of manipulating the substrate by doping it, to induce a structural or dimensionality change in the Au cluster.s

1.3 Theoretical Tools

Depending on the time and length scales involved in the study, many theoretical tools are available to study different phenomena. Theoretical studies of properties of materials became much more practicable and accurate with the formulation of density functional theory (DFT) by W. Kohn, P. Hohenberg and L.J. Sham. [3, 4]. This is one of the most sophisticated techniques currently available to study the quantum many-body problem. It is, in principle, exact, and and in practice it allows the calculation of several properties of the system with reasonable accuracy. These calculations are *ab initio* first-principles electronic structure calculations. The only input is the atomic number of the elements and no other empirical inputs are needed. The DFT technique has been implemented in many packages like SIESTA, VASP, WIEN2k, ABINIT, Quantum-ESPRESSO, etc. We have used the Quantum-ESPRESSO package [5] in the studies discussed in this thesis.

1.4 Outline of the Thesis

This thesis comprises of four chapters. Chapter 2 provides a description of DFT and the techniques related to performing DFT calculations, such as

pseudopotentials, choice of basis sets, smearing, calculation of forces and stresses, etc.

In Chapter 3, we present our studies on surface alloys. The chapter includes an introduction to the subject, the methods used for the study, the discussion of the results we obtained, and finally the summary.

In Chapter 4, we study the morphology of Au_{20} clusters. We have suggested a neat and relatively easy technique to manipulate the substrate such that it controls the morphology of the Au_{20} cluster. This chapter consists of an introduction, methods used, discussion of results and a summary.

In Chapter 5, we conclude by listing out the major results in our work. We also discuss an outlook for future work.

Chapter 2

Density Functional Theory

2.1 The many-body problem

The Schrödinger equation (SE) for a many-body interacting system can be written as given below.

$$\{H_{ion} + H_{el} + H_{ion-el}\}\,\Psi_{tot} = E\Psi_{tot}, \tag{2.1}$$

where the subscripts *ion* and *el* refer to the nuclei and electrons respectively, Ψ represents the wavefunction of the system and E represents the energy eigenvalue of the Hamiltonian. The first two terms H_{ion} and H_{el} are contributions to the Hamiltonian from the nuclei and electrons respectively. They include the kinetic and potential energy terms. The third term H_{ion-el} refers to the interaction between the nuclei and the electrons. The wavefunction Ψ contains all information about the system. Every term in the equation brings

up mathematical complications, and the complexity of the many-body problem makes solving the equation impossible. Three major approximations are applied for an efficient and accurate approach to the problem:

- The Born-Oppenheimer adiabatic approximation for decoupling the nuclear and electronic degrees of freedom.
- Density functional theory for handling the term involving electronic interactions in H_{el}.
- The plane wave pseudopotential approximation which simplifies the calculation of the interaction between the nuclei and electrons in H_{ion-el}.

These approximations are discussed further below.

2.2 Born-Oppenheimer approximation

The difference in mass of electrons and ions lead to faster electronic motion and a comparatively sluggish behaviour of nuclei. By this approximation [6], it is possible to decouple the nuclear degrees of freedom from those of the electrons. If Ψ_i is a set of eigen functions and ε_i are the corresponding eigenvalues which are solutions to the Hamiltonian H when masses of nuclei (M_I) are taken to be very large (or ∞):

$$\left\{ \lim_{M_I \to \infty} H \right\} \Psi_i(\mathbf{R}, \mathbf{r}) = \left\{ \frac{-\hbar^2}{2m_e} \sum_j \nabla_j^2 + V(\mathbf{R}, \mathbf{r}) \right\} \Psi_i(\mathbf{R}, \mathbf{r}) = \varepsilon_i(\mathbf{R}) \Psi_i(\mathbf{R}, \mathbf{r}), \tag{2.2}$$

where m_e is the mass of the electron, V is the potential and $\hbar$ is Planck's constant divided by 2π. $\mathbf{R}$ and $\mathbf{r}$ refer to the positional coordinates of the nuclei and electrons respectively, and j is an index running over all the electrons in the system. The adiabatic approximation [7] states that the particle in the n^{th} eigenstate of the initial Hamiltonian will be carried on to the n^{th} eigenstate of the final Hamiltonian after the Born-Oppenheimer approximation. The approximation improves as the nuclear mass increases. Since the coupling between ground and excited states are minimum, the adiabatic approximation holds true and the total wavefunction $\Psi_{tot}(\mathbf{R}, \mathbf{r})$ can be written as a single term, a function of the ground state wavefunction $\Psi_0(\mathbf{R}, \mathbf{r})$:

$$\Psi_{tot}(\mathbf{R}, \mathbf{r}) \approx \Psi_0(\mathbf{R}, \mathbf{r})\Phi_0(\mathbf{R}). \tag{2.3}$$

The total Hamiltonian within the ground state adiabatic approximation is given by:

$$\left\{ \frac{-\hbar^2}{2} \sum_I \frac{\nabla_I^2}{M_I} + \varepsilon_i(\mathbf{R}) \right\} \Psi_0(\mathbf{R}, \mathbf{r})\Phi_0(\mathbf{R}) \approx E\Psi_0(\mathbf{R}, \mathbf{r})\Phi_0(\mathbf{R}). \tag{2.4}$$

The electronic wavefunction Ψ_0 has a weak dependence on nuclear coordinates and hence all kinetic energy observables of Ψ_0 can be ignored. The nuclear kinetic energy operator acts solely upon the Φ_0 component of wavefunction.

2.3 Density Functional Theory

Several methods were developed to tackle the many-body Schrödinger equation. Physicists developed the diagrammatic perturbation theory, Green's functions and the Hartree-Fock formulation. In chemistry, configuration interaction methods, based on systematic expansion in Slater determinants were used. These latter calculations are expensive computationally and are almost impossible for large and complex systems.

A landmark development in the field of computational science was the formulation of the Density Functional Theory. This enabled the application of electronic structure theory to real problems, and led to the Nobel Prize in Chemistry (1998) for Walter Kohn. Density functional theory represents a complete reformulation of the Schrödinger equation. The many-body N-electron wavefunction is replaced by the electronic density as the basic variable. It makes the problem much simpler as it implies that the electronic density that depends on only position (3 variables) can give us all the information contained in the $3N$-variable quantity wavefunction. Here electron density, which was earlier just an observable of the wavefunction becomes the key variable. The electron density is defined as:

$$n(\mathbf{r}) = N \int d^3\mathbf{r_2} \int d^3\mathbf{r_3} ... \int d^3\mathbf{r_N} \Psi^*(\mathbf{r_1}, \mathbf{r_2}, ..., \mathbf{r_N}) \Psi(\mathbf{r_1}, \mathbf{r_2}, ..., \mathbf{r_N}). \quad (2.5)$$

The prime simplification of the problem relates to considering the many-body interacting system as a one-body non-interacting system by including a term that deals with the exchange and correlation or the many-body effects

of the system.

2.3.1 Hohenberg-Kohn (H-K) Theorem

The Hohenberg-Kohn theorem [8] states that given a ground state density $n_0(\mathbf{r})$, its corresponding ground state wavefunction $\Psi_0[n_0(\mathbf{r})]$ can be calculated. It implies that the external potential can also be estimated from the ground state density within an additive constant. The essence of the H-K theorem lies in the fact that the ground state expectation value of any observable is a functional of $n_0(\mathbf{r})$. Energy, which is the most important observable, can also be written as a functional of the particle density:

$$E_0 = E[n_0]. \tag{2.6}$$

The energy corresponding to the ground state density will always be lower than the energy derived from any other density. If e is the electronic charge, m_e is the mass of the electron and $\mathbf{r_i}$ is the position vector of the i^{th} electron, the energy is given by the expectation value of the electronic Hamiltonian H_e, which is uniquely determinable from the ground state electronic density:

$$H_e = H_{el} + H_{el-ion} = \frac{-\hbar^2}{2m_e}\sum_j \nabla_j^2 + \frac{1}{2}\sum_{j\neq k}\frac{e^2}{\mid \mathbf{r_j} - \mathbf{r_k} \mid} + \sum_j V_{ext}(\mathbf{r_j}), \tag{2.7}$$

where j and k run over the electrons in the system.

$$E_0 \equiv \langle \Psi_0[n_0] \mid H_e \mid \Psi_0[n_0] \rangle = T_{el}[n_0] + E_{el-el}[n_0] + \int V_{ext}(\mathbf{r}) n_0(\mathbf{r}) d\mathbf{r}, \tag{2.8}$$

where the terms T_{el} and E_{el-el} represent the kinetic energy and the interactive potential energy between the electrons respectively and V_{ext} gives the external potential felt by the electrons due to the presence of the nuclei. The nuclear-nuclear interaction potential term is omitted from this expression and can be added later easily.

The H-K theorem further defines a universal functional $F[n]$ which is a quantity independent of the system. The functional $F[n]$ is written as the sum of the internal kinetic and potential energies of the system, and

$$E[n_0] = F[n_0] + \int V_{ext}(\mathbf{r}) n_0(\mathbf{r}) d\mathbf{r}. \tag{2.9}$$

The true form of the functional is unknown and approximations are involved in calculating this term. The external potential energy term is on the other hand exact.

2.3.2 Kohn-Sham Representation

The Kohn-Sham treatment [4] maps the problem of a many-body interacting system onto a single-particle problem. The Schrödinger equation for a non-interacting system is given as:

$$\left\{ \frac{-\hbar^2}{2m_e} \sum_j \nabla_j^2 + V_{ext}(\mathbf{r}) \right\} \psi_i(\mathbf{r}) = \varepsilon \psi_i(\mathbf{r}), \tag{2.10}$$

where ε is the energy eigen value. For an interacting system, two terms considering the Coulomb interaction between electrons as well as the exchange correlation effects in the system are added:

$$\left\{\frac{-\hbar^2}{2m_e}\sum_j \nabla_j^2 + V_{ext}(\mathbf{r}) + V_H(\mathbf{r}) + V_{xc}(\mathbf{r})\right\}\psi_i(\mathbf{r}) = \varepsilon\psi_i(\mathbf{r}), \tag{2.11}$$

or

$$\left\{\frac{-\hbar^2}{2m_e}\sum_j \nabla_j^2 + V_{eff}(\mathbf{r})\right\}\psi_i(\mathbf{r}) = \varepsilon\psi_i(\mathbf{r}), \tag{2.12}$$

where $V_H(\mathbf{r})$ is the Hartree potential which gives the electrostatic interaction between the electrons in the interacting system. The term V_{xc} is a non-classical term that takes into consideration the exchange and correlation effects between the electrons (discussed in the next section). The expression of the Hartree potential is as shown:

$$V_H(\mathbf{r}) = \frac{e^2}{2}\int\int \frac{n(\mathbf{r})n(\mathbf{r}')}{\mid \mathbf{r} - \mathbf{r}' \mid} d\mathbf{r}d\mathbf{r}'. \tag{2.13}$$

It is clear from the equations that the many-body interacting system can be treated like a single-body system with the V_{ext} term being replaced by an effective potential V_{eff} known as the Kohn-Sham potential which includes all the many-body effects. It can be solved exactly like the one-electron system. The ground state charge density, $n(\mathbf{r})$, is expressed in terms of one-electron orbitals (K-S orbitals), $\psi_i(\mathbf{r})$:

$$n(\mathbf{r}) = \sum_i^N \mid \psi_i(\mathbf{r}) \mid^2 . \tag{2.14}$$

where N is the number of electrons. The total energy is given by:

$$E_{HK}[n_0] = T[n_0] + \int V_{ext}(\mathbf{r}) n_0(\mathbf{r}) d\mathbf{r} + \frac{e^2}{2} \int \int \frac{n_0(\mathbf{r}) n_0(\mathbf{r}')}{\mid \mathbf{r} - \mathbf{r}' \mid} d\mathbf{r} d\mathbf{r}' + E_{xc}[n_0], \tag{2.15}$$

where $T[n_0]$ is the kinetic energy corresponding to the ground state density, and $E_{xc}[n_0]$ is the corresponding exchange-correlation energy.

The method of density functional theory is employed by solving the set of equations self consistently. The common procedure followed is listed below.

1. A value of the electronic density is guessed, e.g., from the superposition of the atomic orbitals in the system.

2. The corresponding Kohn-Sham potential is calculated.

3. Using the potential, the Hamiltonian is diagonalized to estimate the Kohn-Sham orbitals $\psi_j(\mathbf{r})$.

4. The newly obtained electronic density is checked for convergence by comparing with the initial guess.

5. A certain combination of the two densities gives a new guess, and the process is repeated until a predefined convergence threshold is achieved.

2.3.3 Exchange-Correlation Functional

The exchange-correlation functional is a term that arises in the Kohn-Sham equations that takes into consideration the many-body effects of the system. Apart from the Coulombic interaction, there exists an effective interaction between electrons due to their spin. The Pauli exclusion principle forbids

two electons of the same spin to co-exist in the same orbital. The interaction between two electrons of like spin is termed the exchange energy, whereas the correlation energy is defined as the difference between the exact energy and the Hartree-Fock energy. The exact formulation of the exchange-correlation functional is not known. The most commonly used forms are the local density approximation (LDA) and the generalized gradient approximation (GGA).

In the local density approximation [9] the system is replaced locally by a homogeneous electron gas with a constant density. The-exchange correlation energy is calculated by integrating over space the energy density e_{xc}^{homo} for a homogeneous electron gas, with the density being replaced by the actual electronic density at each point of the inhomogeneous system:

$$E_{xc}^{LDA} = \int e_{xc}^{homo}[n_0(\mathbf{r})]n_0(\mathbf{r})d\mathbf{r}. \tag{2.16}$$

The exchange-correlation potential is given as the functional derivative of the energy with respect to the electronic density:

$$V_{xc} = \frac{\delta E_{xc}[n]}{\delta n(\mathbf{r})}. \tag{2.17}$$

Initially it was thought that the LDA could be appropriate only to systems with a slowly varying density; however it has been shown to work well even for fairly inhomogeneous distributions. The LDA is exact for a uniform electron gas, but it fails for strongly correlated systems like heavy fermions. It also generally overbinds, i.e., it gives lattice constants that are too small and cohesive energies that are too large.

A modification of the LDA which supplements the density with the gradient of the density, is the generalized gradient approximation (GGA) [10]. It has the general form:

$$E_{xc}^{GGA} = \int e_{xc}^{homo}(n(\mathbf{r}))F_{xc}[\mathbf{r}, n(\mathbf{r}), \nabla n(\mathbf{r})]d\mathbf{r}. \tag{2.18}$$

Here F_{xc} is termed the enhancement factor and is a functional of the electronic coordinates, electron density and the gradient of the electron density. The forms suggested by Perdew and Wang (PW91) [10] and by Perdew, Burke and Ernzerhof (PBE) [12, 13] are two popularly used functional forms of the GGA. They vary in the F_{xc} term. These approximations generally reduce the binding energy, unlike the LDA, thus often leading to better agreement with experiments.

2.4 Plane wave pseudopotential framework

2.4.1 Plane wave basis set

The selection of a basis set to represent a problem is an important step in the wavefunction characterization. For isolated systems such as atoms and molecules, the most commonly used approaches are Gaussian or atomic orbital basis sets. For extended systems, it is convenient to represent them by a basis set of mutually orthonormal plane waves.

In principle, to study an infinite system, a full treatment of the infinite number of electrons is required. The natural periodicity of the lattice saves us from this impossible task. The extended system can be considered as an

infinitely repeating array of supercells. The electrons feel a periodic external potential $V_{ext}(\mathbf{r}) = V_{ext}(\mathbf{r} + \mathbf{R})$, where $\mathbf{R}$ is a lattice vector.

Bloch's theorem states that the wavefunction of an electron placed in a periodic potential can be written as the product of a plane wavefunction and a periodic function as shown below:

$$\psi_{j\mathbf{k}}(\mathbf{r}) = u_{j\mathbf{k}}(\mathbf{r})e^{i\mathbf{k}.\mathbf{r}}. \tag{2.19}$$

Here $u_{j\mathbf{k}}$ is a function that has the same periodicity as the nuclear potential V_{ext} and the exponential term is a plane wave. The additional index $\mathbf{k}$ is used to describe the wavefunction. The wave vector $\mathbf{k}$ is stipulated to lie within the first Brillouin zone. The periodic part $u_{j\mathbf{k}}$ can be expressed in terms of the reciprocal lattice vectors $\mathbf{G}$ as given:

$$u_{j\mathbf{k}}(\mathbf{r}) = \sum_{\mathbf{G}} C_{j\mathbf{k}}(\mathbf{G})e^{i\mathbf{k}.\mathbf{r}}. \tag{2.20}$$

For studying non-periodic systems like surfaces, a certain space of vacuum is added to the repeating cell, such that the atoms do not have a spurious interaction with their periodic images in the next cell. For studying isolated systems, the system can be considered to be in a box of dimensions much larger than its lattice dimensions and calculations are carried for a periodic array of these boxes.

The electronic density of the system can be calculated by summing the square of the norms of the wavefunctions or the occupied Bloch states at a given $\mathbf{k}$ point and then integrating over all k-points within the Brillouin zone:

$$n(\mathbf{r}) = \sum_{\mathbf{k},\mathbf{G}}^{BZ} \sum_{j}^{occ} f_j \mid \psi_{j\mathbf{k}}(\mathbf{r}) \mid^2, \tag{2.21}$$

where j runs over all the ocuupied states of the system. The factor f_j defines the occupancy of the j^{th} state. The size of the basis set $\mathbf{G}$ is infinite, but it can be restricted or decided by a parameter, known as the energy cutoff. The kinetic energy of the plane wave is given by the expression:

$$T_{|\mathbf{k}+\mathbf{G}|} = \frac{\hbar^2 \mid \mathbf{k}+\mathbf{G} \mid^2}{2m}. \tag{2.22}$$

Retaining only those plane waves with a kinetic energy below some predefined cutoff E_{cut} results in a finite basis set.

Plane wave basis sets have advantages over other sets. They are delocalized and independent of atomic positions, making them ideal for calculations on extended systems. They also make the evaluation of energies, forces and stresses easier. Another notable advantage is that the size and quality of the basis set can be controlled by a single parameter, the kinetic energy cutoff. The main disadvantage of using plane waves as the basis set arises due to complications in the core region of the atom. The core electron wavefunctions are highly peaked and the valence electron wavefunctions show many oscillations in the vicinity of the nucleus. This complexity is simplified by creating a pseudo wavefunction with a pseudopotential which mimics the behaviour of the original potential and at the same time, reduces the number of plane waves needed to adequately describe the pseudo wavefunction.

2.4.2 Pseudopotential approximation

The term ion is redefined to include the atomic nuclei as well as the core electrons. The core electrons are tightly bound to the nuclei and contribute very little to chemical bonding. Most of the physical properties of the atom depend on only the valence electrons. Here, the electrons are redefined to refer only to the valence electrons.

The wavefunctions of the valence electrons are altered to remove the oscillations in the core region. A cutoff radius r_c is decided beyond which the pseudo wavefunction is identical to the all-electron wavefunction. The modification of the wavefunction occurs only in the core region where a nodeless pseudo wavefunction capable of reproducing the correct valence behaviour is created.

The problem now remains of obtaining optimal transferability. (A transferable pseudopotential is one that will be effective irrespective of the chemical environment of the atom). As the cutoff radius increases, the number of plane waves for the pseudo wavefunction decreases but leads to poor transferability. Good transferability requires that the pseudo system can replicate the chemical hardness, the excitation energies and the scattering properties of the original system.

Norm conserving pseudopotentials [17] were introduced in 1979 by Harmann, Schluter and Chiang. The norm of the all-electron wavefunction in the core region (0 to r_c) remains conserved in the pseudo wavefunction. The charge of the core, and the scattering properties, are maintained in the pseudo system. This improves the transferability of the pseudopotential.

Another beautiful alternative to the norm-conserving pseudopotential was introduced by Vanderbilt [18] in 1990. Certain atoms like the 2p, 3d and 4f elements have highly localized charge densities in their valence shells as well as the core. The norm conserving pseudopotential then becomes ineffective in reducing the number of plane waves required by the problem. The ultrasoft prescription neglects the norm conserving constraint, generates a smoother function and substantially reduces the size of the required plane wave basis set. It involves multiple reference configurations. The value of r_c can be increased without sacrificing transferability. The ultrasoft pseudopotential is directly involved in solving the Kohn-Sham equations and so the changes in the charge configuration are taken into account in every iteration.

2.5 k-point sampling

The calculation of electronic density or energy involves a continuous sum over every k-point in the system. In principle, there are an infinite number of k-points in the first Brillouin zone (BZ). In practice, it is sufficient to replace the integral with a sum over discrete k-points, usually a Monkhorst Pack grid [19] which is designed according to the symmetry of the system. A uniform set of points is determined using the formula:

$$\mathbf{k}_{n_1,n_2,n_3} = \sum_{i}^{3} \frac{2n_i - N_i - 1}{2N_i}\mathbf{b}_i \qquad (n_i = 1, 2, 3, ..., N_i), \tag{2.23}$$

where N_i is the number of special points in the set and $\mathbf{b}_1, \mathbf{b}_2$ and $\mathbf{b}_3$ are the

primitive reciprocal lattice vectors.

Based on the symmetry of the system, a reduced number of k-points can be chosen. For large supercells the integral can be sampled only at the Brillouin zone origin $\mathbf{k} = (0, 0, 0)$, also known as the Γ point. This is done as the BZ corresponding to a supercell of a perfect crystal contains folded contributions from each component of the unit cell. Single k-point sampling can also be carried out for low symmetry systems, as the inclusion of other points might yield very little information. The accuracy of the Γ point sampling improves as the size of the supercell increases.

For metals, more k-points are required to study the intricate features like crossing of bands. The number can be reduced by employing techniques like smearing or broadening.

2.6 Smearing

The position of the Fermi level with respect to the forbidden gap in the band structure tells us about the nature of the material. In an insulator, the Fermi level lies in the gap, whereas for a metal, it falls where there is a finite (non-zero) density of states. The integration over all k-points for insulators poses no problem and is well behaved, as the density of states goes smoothly to zero before the Fermi level. At finite temperatures the occupancies become continuous similar to the case if the bands were smeared in energy. For finite temperature DFT calculations, Mermin introduced the concept of smearing bands in energy near the Fermi level.

This introduces an entropic term to the total energy and it necessitates

the minimization of the free energy $F = E - TS$ rather than the total energy, where F, T and S represent the free energy, temperature and entropy respectively. If the entropic contribution to the free energy can be accurately calculated, we can always recover the zero temperature result.

The total occupancy in the system is an integral over the occupancies at each k point in the first Brillouin zone:

$$I = \int_{BZ} f(E)[1 - \Theta[E(\mathbf{k}) - E_F]]d\mathbf{k}, \tag{2.24}$$

where $f(E)$ denotes the occupancy of the state, Θ is the Heaviside step function and $E(\mathbf{k})$ is the energy at $\mathbf{k}$. The occupancies will be one or zero depending on whether they lie below or above the Fermi level. For metals, the step function Θ at E_F is very difficult to resolve in plane waves, so it is replaced by a smoother function (an approximation to the delta function) which allows partial occupancies at E_F. So, for metals, the occupancies are smeared or broadened near the Fermi level.

Various techniques are used for this purpose, the common ones being Gaussian smearing, Methfessel-Paxton smearing and Marzari-Vanderbilt cold smearing. In Gaussian smearing [20], the levels are broadened by Gaussian functions. For the Methfessel-Paxton smearing [21] the step function is expanded in terms of Hermite functions which are actually products of Hermite polynomials and Gaussian functions. The major drawback in this method is negative occupation values. This result is unrealistic and causes problems in visualizing density of states.

To treat the problems introduced by negative occupancies, a new method

was developed by Marzari and Vanderbilt [22]. Here the delta function is approximated by a Gaussian function multiplied by a first order polynomial.

2.7 Hellmann-Feynman Forces

The Hellmann-Feynman theorem [23] relates the derivative of energy with respect to a parameter and the expectation value of the derivative of the Hamiltonian with respect to that same parameter. It is given by the expression:

$$\frac{\partial E}{\partial \lambda} = \int \Psi^*(\lambda) \frac{\partial H}{\partial \lambda} \Psi(\lambda) d\tau \tag{2.25}$$

where, the integration is over the domain of the wavefunction with the parameter taken to be λ. The most important application of the Hellmann-Feynman theorem is the calculation of the intramolecular forces in a molecule or extended system.

Earlier, forces were calculated though the agency of energy and its changes with changing configuration of the atoms. To calculate the force on a nucleus in a particular configuration, it was necessary to determine the energy for two or more different and neighbouring configurations. In this way, a plot of energy $vs.$ nuclear coordinates was obtained, the slope of which gave the force on the nucleus. The disadvantage of this method was that it required the calculation of the wavefunctions and energy at the different configurations.

Hellmann and Feynman introduced a new method for the calculation of forces using their theorem with the parameter λ replaced by the nuclear

coordinate. It is designed to obtain forces at a given configuration without the need for calculations at neighbouring configurations. For a system in a steady state, we can define force as the negative of the derivative of the average energy of the system with respect to the nuclear coordinate. If E is the energy of the system with the Hamiltonian H and eigenfunction Ψ, then the force on the nuclei is given by:

$$F_\lambda = -\frac{\partial E}{\partial \lambda} = -\langle \Psi \mid \frac{\partial H}{\partial \lambda} \mid \Psi \rangle \tag{2.26}$$

For a molecule with $1 \leq i \leq N$ number of electrons with coordinates $\mathbf{r}_i = (x_i, y_i, z_i)$ and $1 \leq \alpha \leq M$ number of nuclei with their spatial coordinates $\mathbf{R}_i = (X_\alpha, Y_\alpha, Z_\alpha)$ and nuclear charge Z_α, the Hamiltonian is defined as:

$$H = T + U - \sum_{i,\alpha}^{N.M} \frac{Z_\alpha e^2}{\mid \mathbf{r_i} - \mathbf{R}_\alpha \mid} + \sum_{\alpha,\beta}^{M,M} \frac{Z_\alpha Z_\beta e^2}{\mid \mathbf{R}_\alpha - \mathbf{R}_\beta \mid} \tag{2.27}$$

Only two components of the Hamiltonian contribute to the calculation of force, the interaction terms between electron-nucleus and nucleus-nucleus. Hence, the derivative of the Hamiltonian will be given by:

$$\frac{\partial H}{\partial X_\gamma} = \frac{\partial}{\partial X_\gamma}[- \sum_{i,\alpha}^{N,M} \frac{Z_\alpha e^2}{\mid \mathbf{r}_i - \mathbf{R}_\alpha \mid} + \sum_{\alpha,\beta}^{M,M} \frac{Z_\alpha Z_\beta e^2}{\mid \mathbf{R}_\alpha - \mathbf{R}_\beta \mid}] \tag{2.28}$$

$$= Z_\gamma e^2 \sum_{i}^{N} \frac{x_i - X_\gamma}{\mid \mathbf{r}_i - \mathbf{R}_\gamma \mid^3} - Z_\gamma e^2 \sum_{\alpha \neq \gamma}^{M} Z_\alpha \frac{X_\alpha - X_\gamma}{\mid \mathbf{R}_\alpha - \mathbf{R}_\gamma \mid^3} \tag{2.29}$$

Inserting this into the Hellmann-Feynman expression gives us the x-component of the force on the given nucleus in terms of electronic density

$\rho(\mathbf{r})$ and atomic coordinates and nuclear charges:

$$F_X^\gamma = -Z_\gamma e^2 \int d\mathbf{r}\rho(\mathbf{r}) \frac{x - X_\gamma}{\mid \mathbf{r} - \mathbf{R}_\gamma \mid^3} - \sum_{\alpha \neq \gamma}^{M} Z_\alpha e^2 \frac{X_\alpha - X_\gamma}{\mid \mathbf{R}_\alpha - \mathbf{R}_\gamma \mid^3}. \tag{2.30}$$

2.8 Stress Calculation

A system is said to be in equilibrium when the internal stress equals the externally applied stress. In our work, stress is calculated using a theorem derived by Nielsen and Martin [24–26], where stress is expressed as the derivative of energy with respect to the strain tensor $\epsilon_{\alpha\beta}$ per unit volume. The definition of stress is given by:

$$\sigma_{\alpha\beta} = \frac{1}{\Omega} \frac{\partial E_{tot}}{\partial \epsilon_{\alpha\beta}}, \tag{2.31}$$

where α and β are cartesian coordinates.

2.9 Spin-Polarised Density Functional Theory

Until now, we have considered only the spin-degenerate charge density $n(\mathbf{r})$ of electrons. That is, the number of electrons with up-spin is equal to the number of electrons having a down-spin. Magnetism arises when this number differs. Here, the charge densities of the electrons with up-spin and down-spin need to be considered separately. The charge densities can be written

in terms of the spin-up and spin-down Kohn-Sham orbitals $\psi_i^{\uparrow}(\mathbf{r})$ and $\psi_i^{\downarrow}(\mathbf{r})$ as:

$$n^{\uparrow}(\mathbf{r}) = \sum_i |\psi_i^{\uparrow}(\mathbf{r})|^2,$$
$$n^{\downarrow}(\mathbf{r}) = \sum_i |\psi_i^{\downarrow}(\mathbf{r})|^2. \tag{2.32}$$

The magnetisation density will be given as:

$$m(\mathbf{r}) = n^{\uparrow}(\mathbf{r}) - n^{\downarrow}(\mathbf{r}). \tag{2.33}$$

The charge density $n(\mathbf{r})$ and the three components of the vector $m(\mathbf{r})$ constitute the basic variables of the spin density functional theory. The Kohn-Sham equations then become:

$$\left\{ \frac{-\hbar^2}{2m_e} \sum_j \nabla_j^2 + V_{eff}^{\uparrow\downarrow}(\mathbf{r}) \right\} \psi_i^{\uparrow\downarrow}(\mathbf{r}) = \varepsilon^{\uparrow\downarrow} \psi_i^{\uparrow\downarrow}(\mathbf{r}), \tag{2.34}$$

where the effective Kohn-Sham potential is of the form

$$V_{eff}^{\uparrow\downarrow}(\mathbf{r}) = V_{ext}(\mathbf{r}) + V_H(\mathbf{r}) + V_{xc}^{\uparrow\downarrow}(\mathbf{r}). \tag{2.35}$$

Here, the spin dependent exchange correlation potential $V_{xc}^{\uparrow\downarrow}(\mathbf{r})$ is the functional derivative of the exchange correlation energy $E_{xc}[n^{\uparrow}(\mathbf{r}), n^{\downarrow}(\mathbf{r})]$ with respect to the charge density $n^{\uparrow\downarrow}(\mathbf{r})$.

Like DFT, spin polarised DFT is also, in principle, an exact formulation. Approximations are involved in the exchange-correlation functionals E_{xc} and

$V_{xc}^{\uparrow\downarrow}$ which carry all the many-body effects of the system. The LDA has been modified considering the spin-spin interactions to give the local spin density approximation (LSDA). GGAs for spin polarised systems have also been similarly developed.

Chapter 3

Surface alloys on a W(110) substrate

3.1 Introduction

Alloys are defined as solid solutions of one or more elements in a metallic matrix. The phenomenon of alloying on surfaces to form surface alloys involves a two-dimensional mixing of atoms over a substrate. It can be the mixing of one metal on the surface of another metal, or the mixing of two metals over the surface of a third metal. This can result in periodic or irregular patterns the surface. The properties of these alloys can be drastically different from the alloys in the bulk phase.

The stability of a bulk alloy is governed by a set of rules, called the Hume-Rothery rules [27]. These rules describe the conditions under which one metal can easily dissolve in another metal: (i) the difference in sizes of the atoms should not be more than 15%, (ii) an element with a lower

valency can dissolve more easily in an element with a higher valency; for maximum solubility, the solute and solvent need to be of the same valency, (iii) the crystal structures of the elements should be similar, and (iv) the electronegativity difference between the atoms should not be too much.

In the case of surface alloys, these rules do not seem to hold. Atoms of different sizes are found to form stable surface alloys by means of reducing stress. It was initially believed that if two atoms of different atomic sizes were made to form an alloy over a substrate with its lattice spacing equal to the average of their sizes, they would form stable surface alloys. A seemingly good candidate for such a system might be Co and Ag alloying over Ru(0001). The bond distances in Co and Ag are 2.52 Å and 2.89 Å respectively. The lattice spacing of the substrate Ru is 2.70 Å and is close to the average of the bond distances of Co and Ag. However, experiments [28] on this system show that there is no atomic level mixing between the two species and they form an irregular network of Ag islands in a Co matrix.

The field of surface alloys gained much attention when it was discovered that even bulk-immiscible metals can form stable surface alloys as a result of the different environment at the surface. It was found that Au, being completely insoluble in bulk Ni, replaces Ni surface atoms in the first surface layer forming a surface Au-Ni alloy [29]. Other examples of surface alloys of this kind are monolayer confined mixing at the Ag-Pt(111) interface [30] and Fe atoms embedded directly in the surface layer of a Pt(997) substrate [31]. In both cases the mixing is confined to the topmost layer of the Pt(111) and Pt(997) surface respectively. On the surface, the atoms are poorly coordinated and the bond lengths are different from the bulk.

	Pt	Ag	Au	Cd	Pb
Fe	2.63	2.69	2.68	2.73	2.99
Co	2.64	2.70	2.70	2.74	3.00
Ni	2.63	2.69	2.69	2.73	2.99

Table 3.1: The average of the nearest neighbour bonds, $(a_M + a_N)/2$, for every pair of M and N considered by us. All the values are in Å. Most values are comparable to the nearest neighbour bond length of W in bulk which is 2.76 Å. In this table, all the values used are experimental values [35].

Surface alloys become even more interesting when at least one of the constituents is magnetic, because both the lower coordination at the surface and the change in effective coordination number due to alloying can have a significant impact on magnetic properties [32]. The magnetic moment of the surface alloy per magnetic atom is found to be enhanced compared to the bulk magnetic moment. Lowering of symmetry at the surface, enhanced orbital contribution to magnetism, the narrowing of the d bands and the increased value of the density of states at the Fermi level are reasons for the increased magnetic moment at the surface [33]. An example of such a system is Fe/W(110). Fe has a bulk magnetic moment of 2.2 μ_B, and when placed on W(110) it shows a magnetic moment of 2.56 μ_B [34]. For the purpose of magnetic memory storage devices, it can be convenient to have a surface with patterns of magnetic and non-magnetic domains. For higher storage and stability, a high magnetic moment and high magnetic anisotropy of the system would be desired.

We have chosen eight different metals to consider the formation of alloys over the substrate W(110). Three of the metals, Fe, Co and Ni (M) are small and magnetic and the other five are non-magnetic and belong to a

range of sizes from Pt, Ag, Au, Cd to Pb (N). The metals (M and N) were chosen such that the lattice constant of W lies in between the bulk nearest neighbour (NN) bond distance values of M and N. The average of the bulk NN bond distances of every pair of M and N considered are tabulated in Table 3.1. Most of these combinations of MN are bulk-immiscible except for the alloys with Pt. Different compositions of the alloy and their arrangements are studied. The elastic and the chemical contributions to the stability of the system are extracted separately and looked into.

Earlier studies have been done with different substrates like Ru(0001) [36] and Rh(111) [37]. They have done calculations of the same alloys over these substrates, and analyzed the heat of formation and the magnetic moments of the alloys formed. They have also split the total energy into elastic and chemical contributions and studied their contribution towards the stability of the alloys. A comparison of the alloys over the two substrates was also carried out [38]. The alloys in the cases described were deposited over triangular lattices of the Rh or Ru surfaces. (Rh and Ru have a face centered cubic and hexagonal close packed lattice in the bulk respectively). The coordination number of an isolated atom placed in a hollow site over these surfaces would be three (nine for an atom in a monolayer). In our study we have used another metallic substrate, tungsten. Tungsten has a body centered cubic (BCC) lattice in bulk, and when exposed at the (110) surface, it displays a centered rectangular lattice. An isolated atom placed pseudomorphically above this surface would have a coordination number of only two (six for an atom on a pseudomorphic monolayer). By studying the formation of alloys on the tungsten (110) surface we hope to gain insights on the effects of geometry

and coordination number on the stability and interesting properties of the alloys formed.

Stress is of key importance while discussing effects like forces acting in a surface layer of the metal, surface morphology, surface reconstruction, surface diffusion and adsorbate induced changes of forces between surface atoms. We have considered the stress experienced by the atoms on the W surface to compute its effective size on the surface. The W(110) surface is highly anisotropic [39]. The magnitude of the adsorbate-induced surface stress was therefore found to be different along the [001] and [$\bar{1}$10] directions.

3.2 Method

Bulk and surface calculations were performed using the quantum-ESPRESSO package [5] which is based on spin polarised Density Functional Theory [3]. The Kohn-Sham wavefunctions [4] were expanded in a plane wave basis set with kinetic energy cut off of 40 Ry. Exchange and correlation effects were treated using the Generalised gradient approximation (GGA) [10]. Ultrasoft (Vanderbilt) pseudopotentials were employed to approximate the interaction between the ion cores and electrons [18]. Brillouin zone sums were carried out using Monkhost-Pack meshes [19]. Convergence was aided by using the Methfessel-Paxton smearing [21] technique with the smearing width set equal to 0.05 Ry. All structures were optimised to obtain stable geometries with minimum total energy. To do this, the Hellmann-Feynman forces [23] were calculated and convergence was assumed to have been achieved when forces on all atoms were smaller than 0.001 Ry/Bohr .

Surface properties of the W(110) surface were calculated using a 1×1 cell with one atom per layer. Monolayers of M/W(110) or N/W(110), where M and N refer to magnetic and non-magnetic elements respectively, were constructed and studied using the same cell. A 2×2 cell was constructed when studying binary alloys of the form, M_xN_{1-x}/W(110) where x is the fraction of magnetic metal included. An $8 \times 8 \times 1$ k-point mesh of was used for calculations on the W(110) surface and monolayers over W(110), and a $4 \times 4 \times 1$ mesh was used for systems with alloys over the W(110) surface. For stability and magnetic moments calculations of the alloys on tungsten, an asymmetric slab consisting of four layers of tungsten with one layer of the alloy above, and 11.3 Å of vacuum along the [110] direction, was considered. For stress calculations and evaluation of effective surface sizes of the atoms over the W(110) surface, a symmetric 1×1 slab of six layers of W, with monolayers of atoms on both sides of the slab, and 11.3 Å of vacuum, was considered.

3.3 Results and Discussions

3.3.1 Bulk and Surface calculations on W.

Bulk calculations for tungsten yielded results for the equilibrium lattice parameter to be 3.19 Å. This is close to the experimental value of 3.16 Å. The bulk modulus was calculated to be 296.1 GPa which is in reasonable agreement with the experimental value of 310 GPa [35]. A slab of tungsten with (110) surfaces was considered to study the surface properties. A 1×1 cell

with one atom per layer was constructed for the calculations. Six atomic layers with a vacuum of around 11.3 Å were included in the slab. The surface energy of the slab was computed by the expression:

$$\text{Surface energy} = \frac{E_{slab} - (nE_{bulk})}{2A}, \tag{3.1}$$

where E_{slab} and E_{bulk} are the energies of the relaxed structure of the slab and the bulk, n is the number of layers in the 1×1 slab and A is the area of the cross-section of the slab. It was calculated to be 0.193 eV/Å^2 which is comparable to earlier experimental results [41]. The relaxed inter-layer spacing between the first and second layer, and second and third layer of the W(110) slab were computed to be 2.170 and 2.257 Å respectively. These may be compared to the bulk inter-layer spacing which is 2.256 Å.

3.3.2 Single-component monolayers of different metals over W(110)

Single-component monolayers of magnetic metals Fe, Co and Ni, and non-magnetic metals, Ag, Au, Cd, Pb and Pt, were considered on the W(110) surface. Four different positions of the top layer (relative to the substrate) were considered as shown in Fig. 3.1. In all calculations the monolayer and two W layers beneath it were relaxed in the z direction. The pseudomorphic positions (at the BCC sites) were found to be the most favourable (lowest energy) site in all cases considered. The results of the calculations and the final energies with respect to the most stable configuration for Fe/W(110)

Position	Final Energy (eV)
BCC positions (A)	0.00
top of W (B)	0.926
centroid (C)	0.590
edge (D)	0.425

Table 3.2: Various positions of Fe over W(110) and their corresponding energies. The positions are marked in Fig. 3.1 The pseudomorphic BCC position is found to have least energy, thus making it most stable.

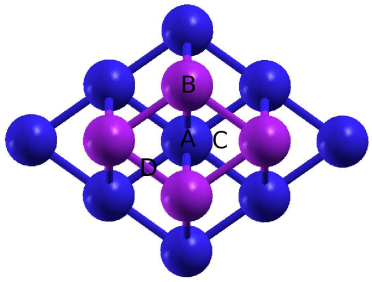

Figure 3.1: The W(110) surface geometry is depicted in this figure. The positions labeled A, B, C and D are the four positions over the substrate considered for monolayer formation over W(110). They are called the pseudomorphic positions, atop W, centroid and edge positions respectively by us. The violet and blue spheres represent the W atoms on the (110) surface. Note the anisotropy of the surface.

are listed in the Table 3.2. The energies, stresses, magnetisation and interlayer distances computed for the monolayers in their stable pseudomorphic positions on the surface on W(110) are given in Table 3.3. For the system Fe/W(110) we obtain a magnetic moment of 2.57 μ_B, which is very close to earlier results of 2.56 μ_B [34]. It is interesting that a monolayer of Ni on W(110) is found to be non-magnetic.

The surface stress experienced by these monolayers of atoms over the W(110) surface was computed. To compute surface stresses, symmetric slabs of six layers of W with monolayers of M or N metals on both surfaces, along

Monolayer	E_{tot} (Ry)	Mag_{tot} (BM/cell)	σ_{xx} (Ry/Bohr^3)	σ_{yy} (Ry/Bohr^3)	d_{12} (Å)
Fe	-692.5424	2.57	-0.000405	-0.000403	1.97
Co	-711.1480	1.40	-0.000513	-0.000476	1.90
Ni	-722.6669	0.00	-0.000335	-0.000237	1.86
Ag	-710.4007	0.00	-0.000185	-0.000276	2.41
Au	-724.5567	0.00	-0.000182	-0.000244	2.39
Cd	-751.5183	0.00	-0.000311	-0.000432	2.54
Pb	-756.9550	0.00	0.000432	0.000231	3.08
Pt	-723.4349	0.00	-0.000261	-0.000207	2.12

Table 3.3: The energies (E_{tot}), magnetisation (Mag_{tot}), stresses (σ_{xx} and σ_{yy}) and the inter-layer distance between the monolayer atom and the W substrate (d_{12}) are listed in the table.

with five layers of vacuum, were considered for calculation. Only the surface atoms M or N were allowed to relax. The surface stress can be extracted from the stresses of the slabs of monolayers on W(110) and the stresses in a similarly oriented and distorted slab of bulk W. The W(110) surface is highly anisotropic, and the surface stress tensor is therefore not symmetric in x and y. For extracting parameters from surface stress calculations, the yy component of the stress tensor was considered. The expression used is derived below:

Consider slabs consisting of atomic layers oriented perpendicular to [110]. Let $\sigma_{\alpha\alpha}^{slab}$ be the $\alpha\alpha$ component of the "volume stress" for the M/W(110) or N/W(110) slabs (it has dimensions of force per unit area, as opposed to surface stress which has dimensions of force per unit length) with n number of atomic layers and length L_z (5 layers of vacuum included) along the z direction. $\sigma^{surf}(l_{xy})$ is the surface stress at an intraplanar bond length l_{xy} and $\sigma_{\alpha\alpha}^{bulk}$ is the $\alpha\alpha$ component of the volume stress for the bulk W cell oriented in the same direction as the slab with the in-plane bond length same as l_{xy}. c is the repeating unit in the z direction in the bulk W. (The

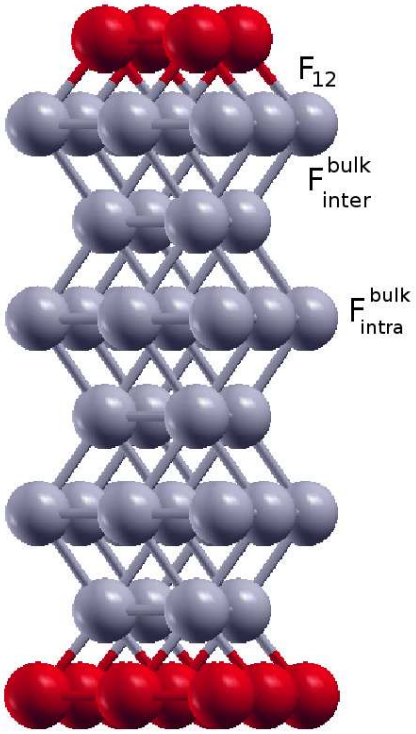

Figure 3.2: A slab of Fe/6 L W(110)/Fe is shown here.The grey and red spheres represent the W and Fe atoms respectively. The bulk inter-planar and intra-planar forces are shown. The inter-planar forces between the monolayer and the bulk W layers is denoted by F_{12} and is labelled in the figure.

repeating unit has a ABAB stacking and so the interplanar distance is given by $c/2$). As an example, Fig. 3.2 shows a slab of Fe/W(110) with 6 W layers and 2 monolayers of Fe. The inter-planar forces between the bulk layers (F_{inter}^{bulk}), inter-planar forces between the monolayer and the W layers (F_{12}) and intra-planar forces in the W layers (F_{intra}^{bulk}) are labelled. Forces only along the nearest neighbour bonds are considered.

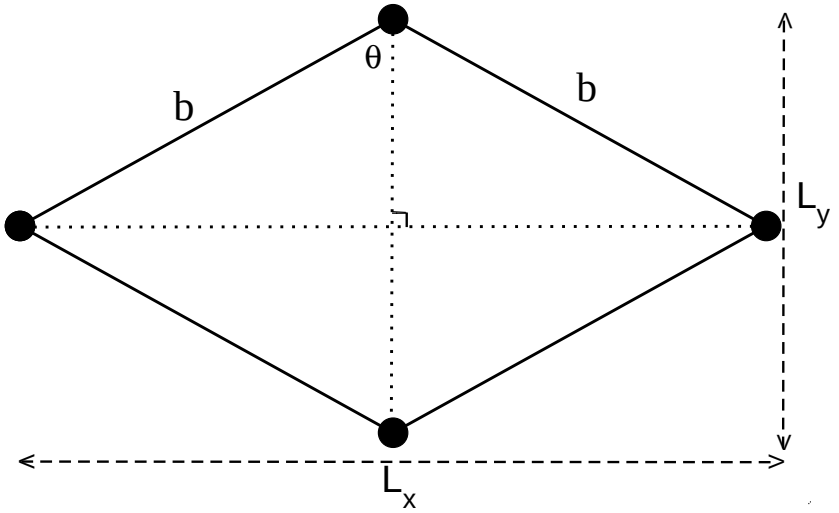

Figure 3.3: The surface geometry of the W(110) surface is shown here. The rhombus formed has an angle (as shown in figure) $\theta = 54.735^o$. The diagonals (or x and y dimensions) are of length $2b\sin\theta$ and $2b\cos\theta$.

$$\sigma_{yy}^{slab} = \frac{F_{y,tot}^{slab}}{L_x L_z} \tag{3.2}$$

$$= \frac{2F_y^{surf} + (n-2)F_{y,intra}^{bulk} + (n-3)F_{y,inter}^{bulk} + 2F_{12}}{L_x L_z} \tag{3.3}$$

$$= \frac{2F_y^{surf} + (n-3)F_y^{tot,bulk} + F_{y,intra}^{bulk}}{L_x L_z} \tag{3.4}$$

$$\sigma_{yy}^{slab} L_z = 2\sigma_{yy}^{surf} + \frac{(n-3)F_y^{tot,bulk} + F_{y,intra}^{bulk}}{L_x} \tag{3.5}$$

For bulk W,

$$\frac{F_y^{tot,bulk}}{L_x c/2} = \sigma_{yy}^{bulk} \tag{3.6}$$

$$\frac{F_y^{tot,bulk}}{L_x} = \frac{c\sigma_{yy}^{bulk}}{2} \tag{3.7}$$

i.e.,

$$\sigma_{yy}^{bulk} = \frac{F_{y,intra} + F_{y,inter}}{L_x c/2} \tag{3.8}$$

$$\sigma_{yy}^{bulk} c/2 = \frac{F_{y,intra} + F_{y,inter}}{L_x} \tag{3.9}$$

$$\frac{F_{y,intra}}{L_x} = \frac{\sigma_{yy}^{bulk} c}{2} - \frac{F_{y,inter}}{L_x} \tag{3.10}$$

$$= \frac{\sigma_{yy}^{bulk} c}{2} - \frac{k_b(b - b_0)cot\theta}{b} \tag{3.11}$$

From the geometry of the surface seen in Fig. 3.3, it can be shown that $F_{y,inter} = 2k_b(b - b_0)cos\theta$, where b_0 is the nearest neighbour distance in bulk W, b is the preferred bond distance (where the surface stress goes to zero), and k_b is the spring constant of the bond considering it as a harmonic oscillator. Here θ is the angle shown in Fig. 3.3 and $L_x = 2bsin\theta$.

In order to obtain an expression for $\frac{k_b(b-b_0)}{b}$ we use:

$$\sigma_{zz}^{bulk} = \frac{F_{z,tot}^{bulk}}{L_x L_y} \tag{3.12}$$

$$= \frac{2k_b(b - b_0)sin\theta}{L_x L_y} \tag{3.13}$$

$$\frac{k_b(b - b_0)}{b} = \frac{4b^2 sin\theta cos\theta \sigma_{zz}^{bulk}}{c} \tag{3.14}$$

Now going to our earlier equation 3.11 we have:

$$\frac{F_{y,intra}}{L_x} = \frac{\sigma_{yy}^{bulk} c}{2} - \frac{4b^2 cos^2\theta \sigma_{zz}^{bulk}}{c}. \tag{3.15}$$

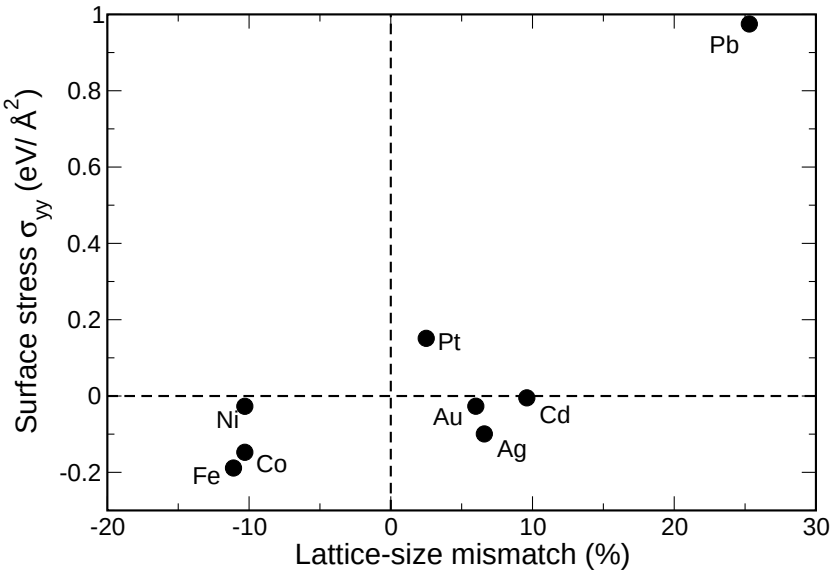

Figure 3.4: The surface stresses σ_{yy} for the single-component monolayers of metals (M or N) on W(110) are plotted as a function of lattice mismatch, defined as $(a-a_s)/(\frac{a+a_s}{2})$, where a is the calculated nearest neighbour distance in bulk metals and a_s is the nearest neighbour spacing in the W substrate.

So now we have,

$$L_z\sigma_{yy}^{slab} = 2\sigma_{yy}^{surf} + \frac{(n-3)c\sigma_{yy}^{bulk}}{2} + \frac{\sigma_{yy}^{bulk}c}{2} - \frac{4b^2cos^2\theta\sigma_{zz}^{bulk}}{c} \tag{3.16}$$

$$2\sigma_{yy}^{surf} = \sigma_{yy}^{slab}L_z - \frac{(n-2)\sigma_{yy}^{bulk}c}{2} + \frac{4b^2cos^2\theta\sigma_{zz}^{bulk}}{c} \tag{3.17}$$

$$\sigma_{yy}^{surf} = \frac{\sigma_{yy}^{slab}L_z}{2} - \frac{(n-2)\sigma_{yy}^{bulk}c}{4} + \frac{2b^2cos^2\theta\sigma_{zz}^{bulk}}{c}. \tag{3.18}$$

For our system, n is 8 atomic layers, with 6 W layers and 2 monolayers with 5 layers of vacuum, so we have:

$$\sigma_{yy}^{surf} = \frac{\sigma_{yy}^{slab}13c}{4} - \frac{6\sigma_{yy}^{bulk}c}{4} + \frac{2b^2cos^2\theta\sigma_{zz}^{bulk}}{c} \tag{3.19}$$

The surface stresses σ_{yy} for M/W(110) and N/W(110) are plotted against

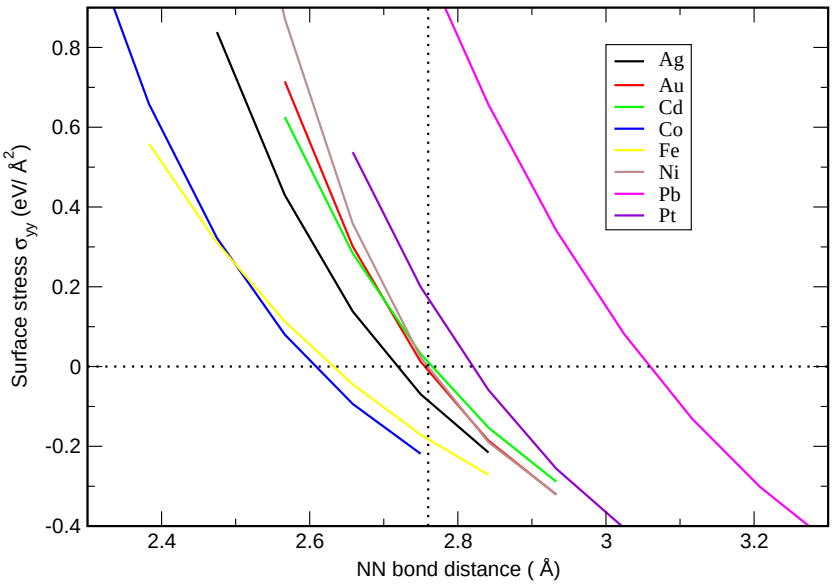

Figure 3.5: Surface stresses σ_{yy} computed for the monolayers of M and N over W(110) are plotted in this graph for varying intra-planar distances. The point where the graph cuts the x axis gives the preferred intra-atomic spacing for the monolayer of M or N. The vertical dotted line shows the nearest neighbour spacing in bulk W.

lattice mismatch of each metal with W(110) in Fig. 3.4. The in-plane distances were then varied, over a range that included both compression and tension. They were distorted isotropically such that the angles between the bonds remained constant, only the bond lengths were stretched or compressed. The inter-layer spacing was kept constant at the relaxed equilibrium spacing between the monolayer and the W layer at l_{xy}. The surface stress σ_{yy} experienced by the atoms at varying lattice spacing in the x-y plane was calculated using equation 3.19 and is plotted in Fig. 3.5 for each monolayer M or N/W(110).

The interaction potential between two NN atoms in the monolayer can

be considered to be of the form of a Morse potential:

$$V_{ij} = A_0^{ij}[1 - exp[-A_1^{ij}(r - b^{ij})]]^2, \tag{3.20}$$

where r is the nearest neighbour distance between the two atoms i and j on the surface, b^{ij} is the equilibrium bond length between i and j, and A_0^{ij} and A_1^{ij} are parameters with the units of potential and inverse of length respectively. As stress can be related to the derivative of the Morse potential, the surface stress graphs of the systems were fitted with the derivative of the Morse potential, and the parameters, A_0^{ij}, A_1^{ij} and b^{ij} were extracted.

The surface stress σ_{yy}^{surf} is given by the expression:

$$\sigma_{yy}^{surf} = \frac{F_y}{L_x}. \tag{3.21}$$

It can be shown that,

$$\sigma_{yy}^{surf} = -\frac{cot\theta}{b}\frac{\partial V}{\partial b} \tag{3.22}$$

$$= -\frac{cot\theta}{b} 2A_0A_1 exp[-A_1(b - A_2)][1 - exp[-A_1(b - A_2)]] \tag{3.23}$$

$$b\sigma_{yy}^{surf} = 2A_0A_1 cot\theta exp[-A_1(b - A_2)][1 - exp[-A_1(b - A_2)]] \tag{3.24}$$

The parameters obtained are listed in the Table 3.4. The Morse potentials for the M-M and N-N bonds when placed over the tungsten slab (at substrate spacing) can be evaluated from these constants.

Metal (M/N)	A_0 (eV)	A_1 (Å^{-1})	b (Å)	a_{bulk}^{calc} (Å)
Fe	9.396	0.573	2.63	2.47
Co	3.223	1.053	2.60	2.49
Ni	2.643	1.440	2.76	2.49
Pt	9.653	0.739	2.82	2.83
Au	3.972	1.124	2.75	2.93
Ag	3.740	1.055	2.72	2.95
Cd	5.536	0.893	2.76	3.04
Pb	18.377	0.528	3.06	3.56

Table 3.4: This table gives the Morse parameters for the interatomic nearest neighbour (NN) bonding interactions (considered as a form of Morse potential) when monolayers of these metals are placed over W(110). The value of b gives the preferred inter-atomic spacing for a monolayer of M or N on W(110) and the last column a_{bulk}^{calc} gives the bulk nearest neighbour spacing.

3.3.3 Alloys of magnetic and non-magnetic metals over W(110)

Using a 2×2 surface unit cell, we have constructed four different configurations of magnetic-nonmagnetic metal alloys on the tungsten(110) substrate (four layers of W considered) as shown in Fig. 3.6.

It is interesting to note that there are two possible arrangements for the 50% compositions, namely the striped and the checker-board arrangement. Calculations were done allowing the alloy atoms and two layers of W beneath it to relax in the z direction. Spin polarised calculations were carried out to study the magnetization of the resulting surface alloy.

Stability of Surface alloys, Enthalpy of Formation

The enthalpy of formation for the surface alloys was calculated using:

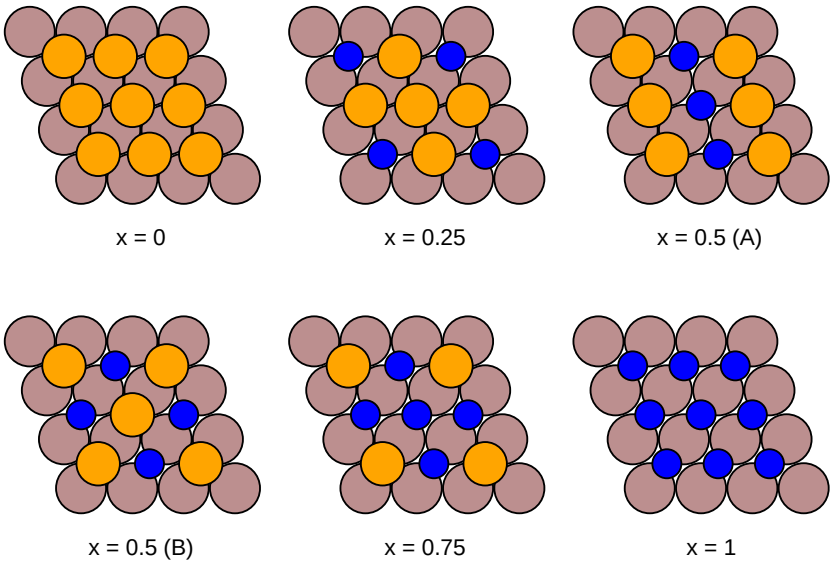

Figure 3.6: A top view of the systems with different compositions of the alloys $M_xN_{(1-x)}/W(110)$ and their arrangements over the 2×2 cell of the W slab considered by us. The brown spheres represent the W surface, and the blue and orange spheres show the positions of the magnetic and non-magnetic atoms respectively.

$$\Delta H = E(M_xN_{1-x}/S)/4 - xE(M/S) - (1-x)E(N/S), \tag{3.25}$$

where $E(M_xN_{1-x}/S)$, $E(M/S)$ and $E(N/S)$ are the total energies of the relaxed structures of the alloy $M_xN_{1-x}/W(110)$, and monolayers of the magnetic and non-magnetic atoms, respectively, over the tungsten slab.

Fig. 3.7 shows the calculated enthalpy of formation for all the alloys. The more negative the enthalpy of formation is, the higher is the miscibility. It can be observed from the graph that a few of the metals like silver and gold in their 50% composition with the magnetic metal prefer the striped arrangement. The metals like lead and platinum seem to be more stable in

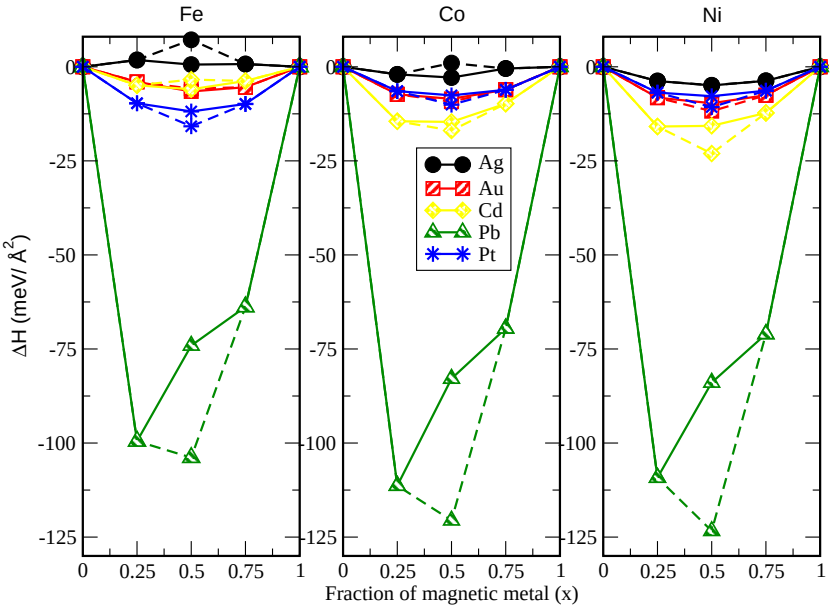

Figure 3.7: Enthalpy of formation of alloys of various compositions. Solid lines go through the $x = 0.50$ striped arrangement, while the dashed lines go through the $x = 0.50$ checker-board configuration.

the checker-board arrangement. Surprisingly, cadmium is found to prefer the striped arrangement in the alloy with Fe whereas it favours the checker-board arrangement when alloying with Co and Ni. Alloys of Ag are found to give positive enthalpy of formation for most compositions, rendering them to be the least stable among all the alloys.

Elastic and Chemical contributions

The stability of such surface alloys is generally determined by two main contributions: elastic interactions and chemical interactions between the atoms on the surface [36]. To study these contributions it is first necessary to separate them out from the total energy.

The elastic energy for the various compositions can be expressed as the

sum of interaction energies of all the NN bonds in the cell, including the M-M, N-N and M-N bonds. For the structures considered by us, the relations giving the elastic contribution to the formation energy can be derived and are as follows:

$$\Delta H^{ela}_{0.25} = 4V_{MN}(a_s) - 2V_{MM}(a_s) - 2V_{NN}(a_s), \tag{3.26}$$

$$\Delta H^{ela}_{0.5striped} = 4V_{MN}(a_s) - 2V_{MM}(a_s) - 2V_{NN}(a_s), \tag{3.27}$$

$$\Delta H^{ela}_{0.5checker-board} = 8V_{MN}(a_s) - 4V_{MM}(a_s) - 4V_{NN}(a_s), \tag{3.28}$$

$$\Delta H^{ela}_{0.75} = 4V_{MN}(a_s) - 2V_{MM}(a_s) - 2V_{NN}(a_s). \tag{3.29}$$

where ΔH^{ela}_x is the elastic contribution to the total energy for a composition of $M_xN_{(1-x)}$. $V_{MN}(a_s)$, $V_{MM}(a_s)$ and $V_{NN}(a_s)$ are the Morse potential values for M-N, M-M and N-N bonds when the in-plane spacing is the equilibrium W substrate spacing a_s. Note that the equations 3.26, 3.27 and 3.29 are identical. To evaluate the potential between the M and N atoms, we need to extract the Morse parameters for the M-N bonds from the M-M and N-N parameters we know. In analogy with the Lorentz-Berthelot mixing rules, we have the expressions:

$$A_0^{MN} = \sqrt{A_0^{MM} A_0^{NN}}, \tag{3.30}$$

$$A_1^{MN} = \sqrt{A_1^{MM} A_1^{NN}}, \tag{3.31}$$

$$b^{MN} = \frac{b^{MM} + b^{NN}}{2}. \tag{3.32}$$

b^{MN} (Å)	Ag	Au	Cd	Pt	Pb
Co	2.66	2.68	2.68	2.71	2.83
Fe	2.68	2.69	2.70	2.72	2.84
Ni	2.74	2.76	2.76	2.79	2.91

Table 3.5: This table gives the values of b^{MN} for every pair of M and N. It is the average of the preferred nearest neighbour spacing on the surface.These values can be compared to our calculated value of 2.76 Å for the NN distance on the W substrate.

Here, A_0^{ij}, A_1^{ij} and b^{ij} are the Morse parameters for an i-j bond, where i and j can be M or N. The average of the preferred atomic spacings of every pair of magnetic and non-magnetic metals is calculated and is shown in Table 3.5. This gives us an idea of the inter-atomic spacing the atoms of the alloys will adopt so as to minimize the elastic energy.

The individual contribution of the Morse potential terms to the total elastic contribution for the $x = 0.25$ (3.26), $x = 0.5$ (3.27, striped arrangement and $x = 0.75$ (3.29 compositions of the alloys are shown in Fig. 3.8. Pb-Pb bonds are found to have a high negative contribution to the elastic contributions to the energies of its alloys.

The graphs which show the elastic contribution to the formation energy in the various systems is shown in Fig. 3.9. It can be seen clearly that all the alloys except Ni-Ag have a negative elastic energy contribution. The contributions for 25%, 50% (striped) and the 75% alloys are the same as the number of nearest neighbour MN bonds in the surface are the same. The checker-board arrangement in the 50% alloy involves formation of double the number of M-N bonds, and hence we see a higher contribution of the elastic interactions towards the stability of these alloys.

The chemical contribution to ΔH can be calculated as the difference

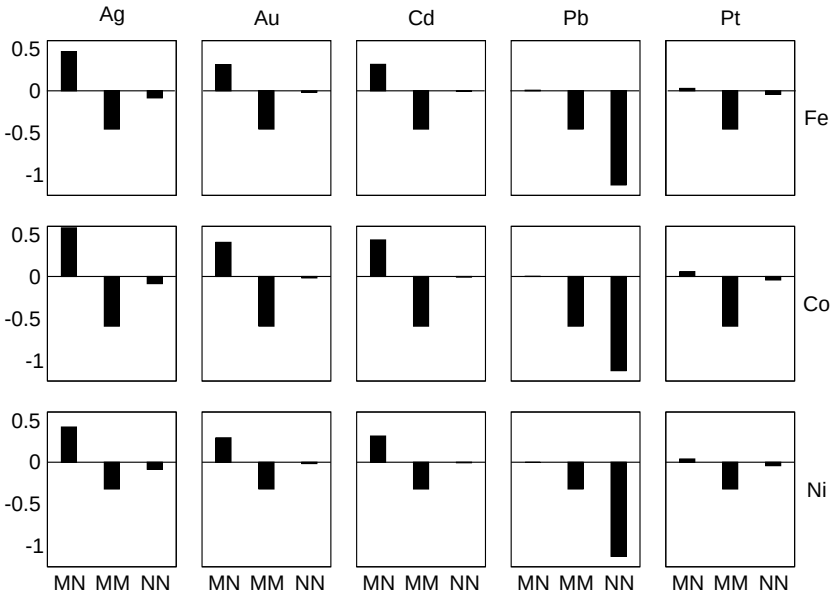

Figure 3.8: The contributions of the individual terms ($4V_{MN}$, $-2V_{MM}$ and $-2V_{NN}$) in the elastic interaction for the $x = 0.25$, $x = 0.50$ (striped arrangement) and $x = 0.75$ compositions of the alloys are shown above. The first row shows the alloys of Fe, the second and third rows show the alloys of Co and Ni respectively. All the histograms have been plotted on the same scale, to make comparision easier. Pb-Pb bonds show a very high negative contribution to the elastic energy its alloys

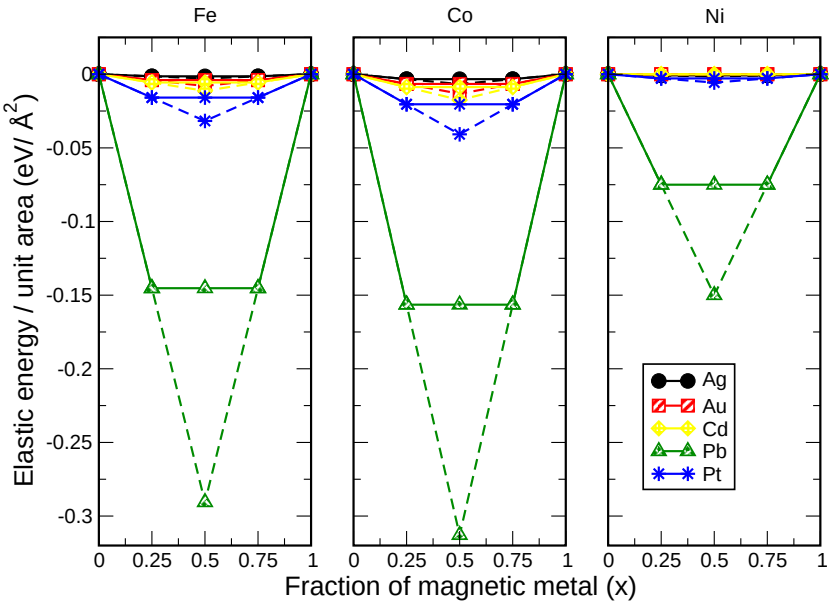

Figure 3.9: Elastic contributions to the formation energies of the alloys.

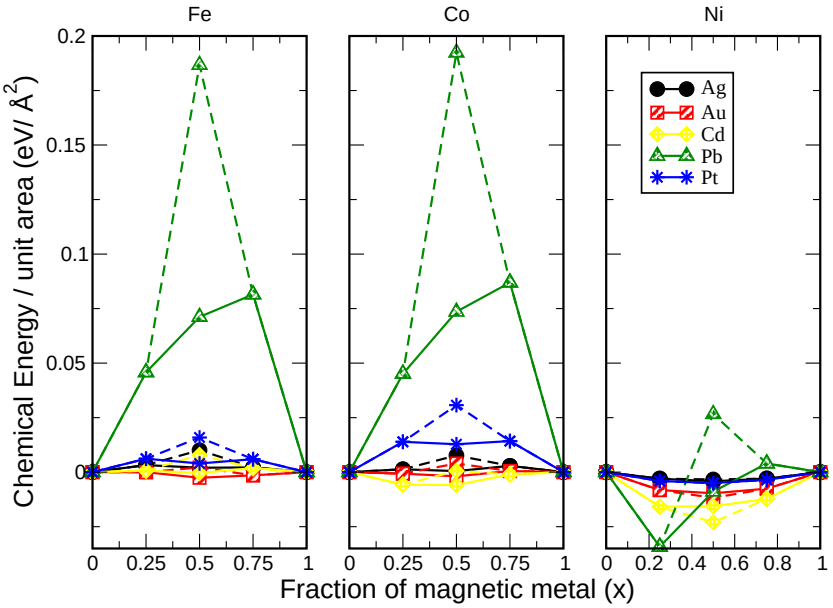

Figure 3.10: Chemical contributions to the formation energies of the alloys.

between the enthalpy of formation and the corresponding elastic contribution to ΔH:

$$\Delta H_x^{chem} = \Delta H_x - \Delta H_x^{ela}. \tag{3.33}$$

The chemical contributions to the formation energies computed for all the systems are presented in the graph in Fig. 3.10. Here we can see that for the checker-board arrangement of the 50% alloy, the chemical interaction terms are highly positive. The formation of the chemical bonds in the Fe and Co alloys is unfavourable. In the case of the Ni alloys, the alloys with Ag, Au and Cd are found to have a favourable chemical interaction contribution to the stability of the alloys.

Magnetic Moments

It is expected that the magnetic moment of a magnetic metal increases when placed upon a non-magnetic substrate. The bulk magnetic moments of Fe and Co are 2.2 and 1.7 μ_B respectively and are found to be altered to 2.57 μ_B and 1.4 μ_B respectively when placed over W(110). Alloying of these metals with non-magnetic metals leads to changes in the value of magnetic moments and a general trend of decreasing moments with decreasing percentage of magnetic atom can be observed. Only alloys of Fe and Pt as well as Fe and Au (25% and checker-board 50% arrangement) seem to show higher magnetic moment than Fe monolayers over W(110). Generally the checker-board arrangements seem to cause a higher moment than the corresponding striped arrangements with the exceptions of Fe-Pb, Fe-Cd and Co-Pb. The

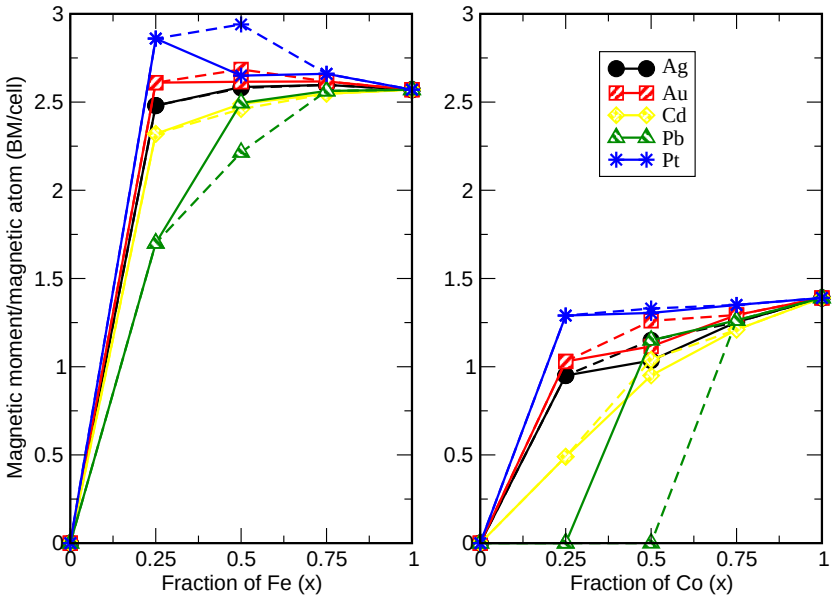

Figure 3.11: Magnetic moments of the alloys constructed. Note that the monolayer and most alloys of Fe show a higher magnetic moment per Fe atom than the bulk Fe magnetic moment of 2.22 μ_B. The monolayer of Co and its alloys show a lower magnetic moment per Co atom than the bulk Co magnetic moment of 1.7 μ_B

differences between the magnetic moments of the two 50% arrangements are more pronounced in the Co alloys than in the Fe alloys, except in the case of Pt, as can be seen from Fig. 3.11. Ni which has a low bulk magnetic moment of 0.6 μ_B when placed over W(110), gives zero magnetic moment. This is a surprising result.

We tried to understand the factors governing the stability of the striped and checker-board arrangements. A graph depicting the effective coordination of the atoms in the two configurations, their stability and their magnetic moment is seen in Fig. 3.12.

By projecting the charge density onto atomic orbitals, the moments on individual atoms can be extracted. We find an anti-ferromagnetic interaction

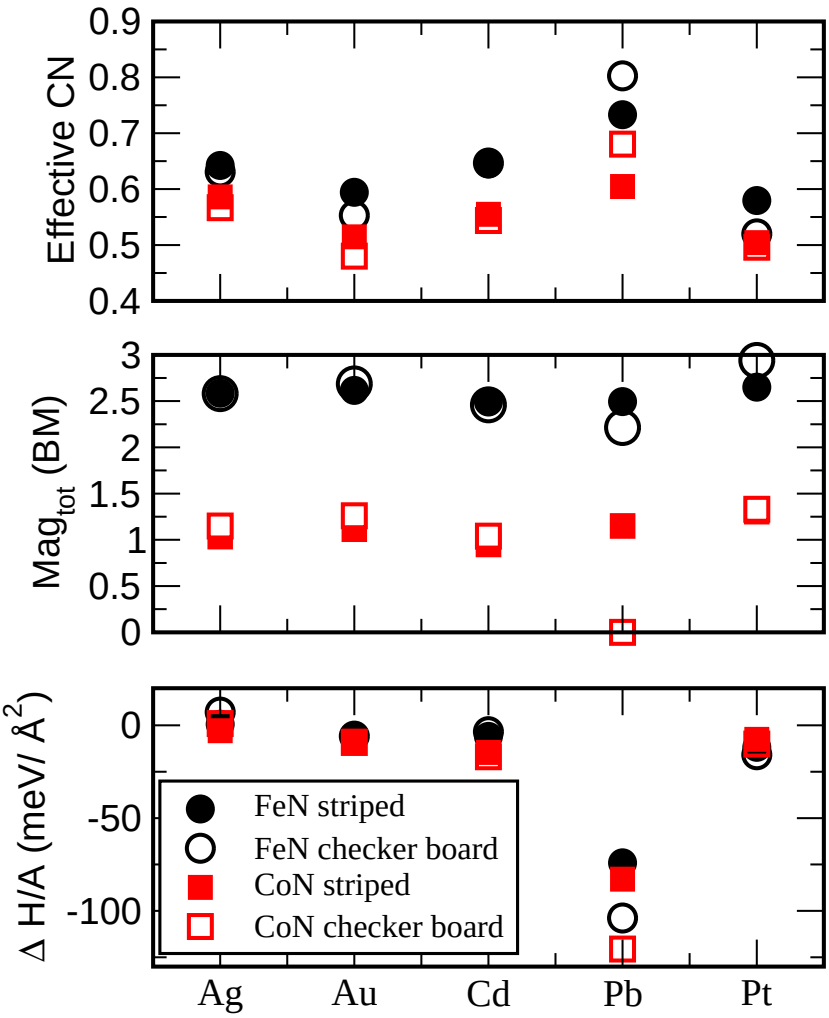

Figure 3.12: To study relationships between the magnetic moment, effective coordination number, and the stability of the striped and checker-board arrangement. We can see that smaller the effective coordination number of the atoms in a configuration, the greater will be its magnetic moment. No such trend was observed for the stability and magnetic moment of these configurations. Here CN, Mag_{tot} and Δ H/A represent the effective coordination number, total magnetisation of the system per magnetic atom and the enthalpy of formation of the alloy per unit area.

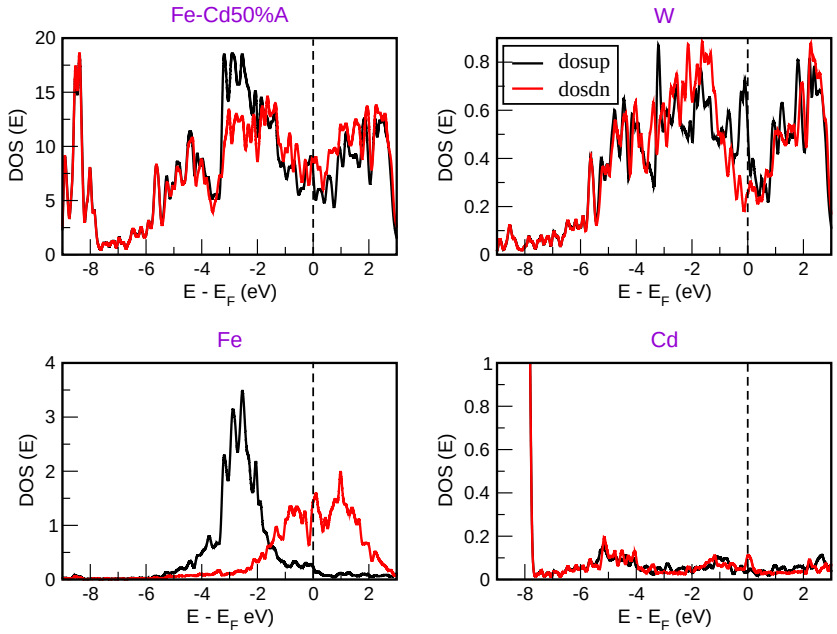

Figure 3.13: The individual density of states of the magnetic atom and the substrate atom reveal the anti-ferromagnetic interaction leading to the low magnetic moments in the alloys. The black and red lines show the up and down spin density of states. The vertical dotted line represents the Fermi level in the system. At the Fermi level, it can be seen that W has a high up-spin density of state, the Fe atom has a high low-spin density of state.

between the W atoms and the magnetic atom. The relatively low magnetic moment obtained from the surface alloys on W(110) compared to surface alloys on other surfaces like Ru(0001) and Rh(111) [38] may be attributed to this finding. As an example, the density of states for the magnetic atom, non-magnetic atom and the magnetized substrate atoms are shown in Fig. 3.13 for the striped arrangement of the Fe and Cd alloy.

3.3.4 A comparative study: magnetism of the surface alloys on Ru and Rh substrates

Comparing our results on surface alloys over W(110) with earlier results on different substrates Ru(0001) and Rh(111) [38], we find that the effect of the substrate in determining the miscibility of the surface alloys is not very significant. In all three cases, we find that the mixing at the atomic level is not favoured for Ag alloys, all other combinations have a negative enthalpy of formation.

The preferred surface sizes of the of Fe and Co were found to be larger on the W(110) than the sizes preferred on Ru(0001), where as the non-magnetic metals except Pt were found to prefer smaller surface sizes on W(110) than Ru(0001) [36]. The coordination numbers of atoms in the monolayers over W(110) and Ru(0001) are 6, 9 and 9 respectively.

Upon placing monolayers of Fe and Co on the substrates, the net magnetic moments are found to be significantly largest for Fe and Co on Rh(111) (3.32 and 2.67 μ_B respectively). On Ru(0001), the moments are found to be 2.80 and 1.83 μ_B respectively for Fe and Co. The least magnetic moment is found for Fe and Co on W(110), 2.57 and 1.4 μ_B respectively.

3.4 Summary

We have found that bulk-immiscible metals form stable alloys on the surface of W(110). The surface sizes of the atoms over the W(110) layer were shown to be different from their bulk sizes. The nearest-neighbour (NN) spacing

of W is slightly larger than the NN spacing in Ru and Rh, but the surface sizes adopted by the metals over the W(110) surface were found to be smaller than their corresponding sizes on Ru(0001) and Rh(111). This is presumably because of the lower coordination on the W(110) surface. The effective atomic sizes were found to be larger than the bulk sizes in magnetic atoms and smaller than their bulk sizes in non-magnetic atoms.

The magnetic moment of the monolayer of Fe on W(110) (2.57 μ_B) was found to be higher than its bulk magnetic moment ($2.2\mu_B$). This is in close agreement to earlier results [34]. The antiferromagnetic interaction of the Fe layers with the W substrate and the non-magnetic metal reduces the magnetic moment considerably in the alloys. All alloys of Co show a lower magnetic moment per Co atom that the bulk magnetic moment of 1.7 μ_B.

We found that there are three main factors determining the stability of a surface alloy: (1) the elastic interaction between the atoms of the alloy on the surface, (2) elastic interaction of the phase segregated monolayer on W(110) and (3) the chemical interaction between the atoms forming the alloy on the W(110) surface. A simple analogy of the Hume-Rothery rule relating the size of the atoms and the miscibility could not be established for surface alloys.

Chapter 4

Controlling morphology of Au clusters by substrate doping

4.1 Introduction

Until the late twentieth century, gold was considered to be unreactive and noble. The importance of gold in society is related to the very fact that it is the least reactive of all metals. The unreactive property of bulk gold or extended gold surfaces is not however due to the inability to form chemical bonds. Gold is found to form very stable alloys with many metals. A study on the nobleness of gold [42] led to the understanding that the inertness of the material in forming bonds at the surface is due to two factors: (i) the degree of filling of the antibonding states on adsorption and (ii) the degree of orbital overlap with the adsorbate. Previous authors have studied the reactivity of extended transition metal surfaces like Ni, Cu, Pt and Au for H_2 molecule adsorption [42]. The reaction can be divided into a simple two-level

problem. First, the interaction of the H 1s state with the 4s or 6s state of the metal leads to a low energy bonding state and an empty antibonding state. This causes an attractive interaction between the metal and the H_2 molecule for all four metals. The next step is the interaction of the bonding state with the metal d states. This shifts the bonding state further lower and the antibonding state higher above the metal d bands. The d-shell configurations of Cu and Au are such that these antibonding orbitals get filled, resulting in a repulsive interaction. The hybridization of two orbitals dictate that they are orthogonal to each other and to make two orbitals orthogonal to each other, it requires energy. This orthogonalization energy increases with the orbital coupling matrix element. In the case of Au, the extended 5d states increase the magnitude of the coupling matrix element and thereby increase the orthogonalization energy cost.

The position of gold in the periodic table is unique. The d-shell filling increases when moving to the right along the transition metals in the periodic table. On reaction with any atom or molecule with a filled one-electron level below the Au d bands, the antibonding orbitals get filled and hence they create weak bonds. The size of the coupling matrix element increases down the group in the periodic table making the 5d metals the least reactive. The ability of Au to break the intermetallic bonds determines its tendency to form bulk compounds like oxides, carbides or hydrides or even alloys. This introduces a new factor, i.e., the cohesive energy of the metal. In the periodic table, the 5d metals have the largest cohesive energy. Considering these three factors, Au can be considered as the least reactive metal among all the other transition metals.

For a long time, Au was considered to have very low catalytic activity and therefore only its co-ordination and organometallic compounds were investigated intensively. In 1935, for the first time, AuCl and $AuCl_3$ were found to catalyse the chlorination of naphthalene to octachloronaphthalene [43]. These were further used for many organic syntheses. A surprising finding which changed the field of Au catalysis was made by Haruta and his coworkers. They found gold nanoparticles supported on semiconducting transition metal oxides catalysing CO oxidation efficiently at low temperatures [44]. This drew a lot of interest towards these unrecognised properties of gold. Small nanosized particles of Au were found to have different physical and chemical properties than their bulk counterparts.

Mass spectra of clusters show a pronounced intensity for certain numbers of atoms, and these numbers of atoms have been termed magic numbers. The origin of the magic numbers may be due to electronic or geometric structural stabilization of the Au core. It is known that the magic numbers for free Au clusters are 8, 18, 20, 34, 40, 58, 92, 138,..., which is explained in terms of closure of the electronic shells created by spherical potentials [45, 46]. The Au_8 cluster was found to be the smallest cluster which was both stable and catalytically active [47]. The Au_{20} cluster was also found to be highly catalytically active due to its electronegativity [48]. Experimental studies on these clusters by photoelectron spectrocopy revealed that this cluster has an extremely large energy gap and a high electron affinity [48]. These observations suggest that a 20-atom Au cluster should be highly stable and chemically inert. This property is an important criterion for a cluster to be used as a potential building block for cluster-assembled materials. The

large energy gap between the highest occupied molecular orbital (HOMO) and the lowest unoccupied molecular orbital (LUMO), and a closed electron configuration, also lead to the chemical stability of the cluster. The HOMO-LUMO gap was measured to be 1.77 eV and the electron affinity of the cluster was found to be 2.745 eV [48]. Relativistic density functional theory calculations found that the Au_{20} clusters possess a tetrahedral structure [48], which is a fragment of the face-centered lattice of the bulk gold with a small structural relaxation.

As size selective methods of preparation of these clusters have become possible, there has been a huge wave of research towards the study of these clusters, their nature, stability and structures. Au clusters were found to be oxidation resistant [49], they were found to enable selective binding of DNA [50] and have potential applications in nanoelectronics [51]. The catalytic property of Au_{20} clusters was found to be desirable for many oxidation reactions. This led to the study of how one can improve the catalytic properties of the clusters by; (1) manipulating the atomic structure, morphology and shape of the catalyst; (2) changing the support (composition, structure and thickness) [52, 53] or (3) the application of external electric fields [54]. Changing any of these characteristics of the system may alter the adsorption energies and the reaction barriers involved in the catalytic reaction.

Studies were carried out to understand and control the various properties of these clusters. The Au_{20} cluster was found to be extremely robust to distortions when supported over an MgO surface, keeping its tetrahedral structure [55]. The catalytic CO oxidation by Au was studied as a function of the charged state of the cluster, and it was observed that while the neutral

cluster was only moderatively active, the negatively charged cluster showed excellent CO conversion yields and rates [55]. Molecular oxygen adsorbing on the surface of the negatively charged Au atoms gets activated to a peroxo state via the occupation of the antibonding $2\pi^*$ orbital. An attempt to create negatively charged Au clusters involved the introduction of F-center defects in MgO, making it very defect-rich. These defects act as anchor sites for the cluster and also initiate a charge transfer towards the cluster, making it slightly negative. The negatively charged cluster was found to be catalytically more active than its neutral counterpart [56].

It was predicted that CO oxidation by Au clusters may be enhanced if the ground state tetrahedral geometry of the Au_{20} cluster could be changed to a flat or two-dimensional structure [53]. Many attempts have been made to control the geometry of the clusters. Au_{20} clusters were supported on MgO over Mo(100) (which is a low work-function metal), and the clusters were found to prefer a two-dimensional planar geometry (P) over the stable tetrahedral structure (T) with an energy difference of 3.3 eV [57]. The thin film of MgO (1-7 layers) enables a charge tunneling from the Mo substrate, through the MgO film to the Au_{20} clusters. The charge transfer to the T and P clusters were calculated to be 1.06 and 1.62 e respectively. The increased number of contacts with the substrate leading to a larger accumulation of interfacial charge, and the electrostatic attraction between the negatively charged Au atoms and the underlying metal, may be the source of the stabilization for the planar geometry. Further methods were sought out to control the morphology of these Au_{20} clusters, One of them included the application of electric field (in a calculation) when the cluster was placed

over MgO supported on Ag(100) [54]. On bulk MgO, and for more than 7 layers of MgO/Ag(100), the T cluster was found to be more stable. The effect of many layers of MgO on Ag was reversed in a field of 1 V/nm where the planar cluster placed on MgO (8 layers) / Ag(100) was found to be favoured over the tetrahedral structure of the cluster.

In this work of ours, we have proposed a method to control the morphology of the cluster by doping the MgO substrate with Al atoms. Doping of the substrate is a relatively much easier method of preparation than preparing thin films of MgO on metals. We find that the doping of the MgO causes similar effects to that of a thin layer of MgO on Mo(100). The charge transfer from the substrate to the Au_{20} cluster allows it to lie flat over the substrate. We also show that a linear relation exists between the dopant concentration and the energy difference between the P and T configurations.

4.2 Method

We have employed Density Functional Theory (DFT) [3] as the method to study the charged state and the shape selectivity of the Au_{20} clusters over the doped magnesium oxide substrate. The quantum-ESPRESSO package, [5] within the framework of spin-polarised DFT was used. The Kohn-Sham wavefunctions [4] were expanded in a plane-wave basis set with a plane-wave energy cut off of 30 Ry and a charge density cut off of 240 Ry. For the self consistent calculations, convergence was assumed to be achieved when the estimated energy error was less than 10^{-8} Ry. The exchange-correlation effects

were treated with the generalised gradient approximation (GGA) (Perdew-Wang 91) [58]. The pseudopotentials used to approximate the interactions between the core and the valence electrons were ultrasoft (Vanderbilt) pseudopotentials [18]. Scalar relativitic pseudopotentials were used for Au atoms.

All calculations on the doped system with and without the cluster were hastened by smearing the occupations using Marzari-Vanderbilt cold smearing [22] with a broadening width of 0.068 eV.

All atoms in the calculations were relaxed. The forces on the atoms were calculated by the Hellmann-Feynman theorem [23]. The convergence criterion for the ionic minimization was satisfied when all components of the forces on the atoms were less than 10^{-3} Ry/Bohr and the energy difference between two consecutive ionic steps was less than 10^{-4} Ry.

MgO has a face centered cubic (FCC) crystal system. The MgO(001) surface was considered as the support for the gold cluster adsorption. This surface can be considered as a square lattice with a two-atom basis. The properties of bulk MgO and aluminium-doped MgO were compared using a $3 \times 3 \times 3$ cell. The doped MgO was created by replacing one of the 27 Mg atoms by Al, resulting in a dopant concentration of 3.7 %. The calculations on the 20-atom clusters of gold were carried out with the Makov-Payne correction [59]. This is employed when the system needs to be considered as an isolated system. The measurements on the Au_{20} cluster adsorbed on the MgO (doped and undoped) were carried out on a 6×6 surface unit cell of 4 layers, with 36 atoms of Mg and 36 atoms of O per layer. The Au_{20} clusters were placed directly above one of the Al atoms in the substrate. A vacuum of thickness around 14 Å in the [001] direction (distance calculated from the

top of the Au cluster to the bottom of the next repeating slab) was used for these calculations. Due to the artificial perriodicity generated by the slab calculations, all calculations done with the clusters on the slabs were done with a dipole correction to the cell [60].

In order to compare with the calculations of previous authors, we also performed a few calculations on metal-supported thin films of MgO. A system with four layers of Mo(100) and a single layer of MgO was used. The O atoms were placed above the Mo atoms, and the Mg atoms occupied the body centered cubic pseudomorphic positions. Calculations on the slab were carried out on a 1×1 cell. In all calculations, the bottom two layers of Mo was considered static and all other atomic coordinates were relaxed.

k-point sampling for the cells with the clusters was done only at the zone center, whereas the sampling for the unsupported slabs of undoped MgO were done using a $2 \times 2 \times 1$ Monkhorst-Pack mesh [19].

4.3 Results

4.3.1 Bulk calculations on pure and Al-doped MgO, Au and Mo.

The FCC lattice constant for bulk MgO was computed to be 4.26 Å which is close to the experimental value of 4.21 Å. The bulk modulus of MgO was found to be 146.3 GPa which is in reasonable agreement with the experimental result of 155.0 GPa [35]. The bulk calculations on Au (FCC lattice) yielded results of lattice parameter and bulk modulus to be 4.15 Å and 144.3

GPa, compared to the experimental results of 4.08 Å and 180.0 GPa respectively [35]. We also computed the bulk lattice constant and bulk modulus of Mo (which has a body centered cubic lattice) to be 3.21 Å and 264.6 GPa respectively, which are in good agreement with the corresponding experimental values of 3.15 Å and 230 GPa.

Two dopant concentrations of Al in the pure MgO system were considered. In the first case, one Mg atom out of a $2 \times 2 \times 2$ cell was replaced by Al giving a concentration of 12.7%. In the second case, one Mg atom out of a $3 \times 3 \times 3$ cell was replaced by Al, giving a concentration of 3.7%. As we will show below, the extra electron is delocalised and its main effect is to shift the Fermi level. Qualitatively similar results are obtained for dopant concentrations of 12.7 % and 3.7 %.

Fig. 4.1 shows the band structures of the undoped primitive cell of bulk MgO and a $3 \times 3 \times 3$ cell of 3.7% Al-doped MgO. From the graphs, we can see that MgO is surely an insulator with a direct gap of around 4.78 eV. The experimental value of the band gap is around 7.8 eV. The underestimation of band gaps is a well known feature of DFT, as is seen in this case. In the case of the doped system, we can observe a clear shift in the Fermi level of about 1.39 eV into the conduction band.

The density of states (DOS) for these systems is plotted in Fig. 4.2. The DOS is more or less unchanged upon doping with Al; the main effect of the doping is to shift the position of the Fermi level into the conduction band.

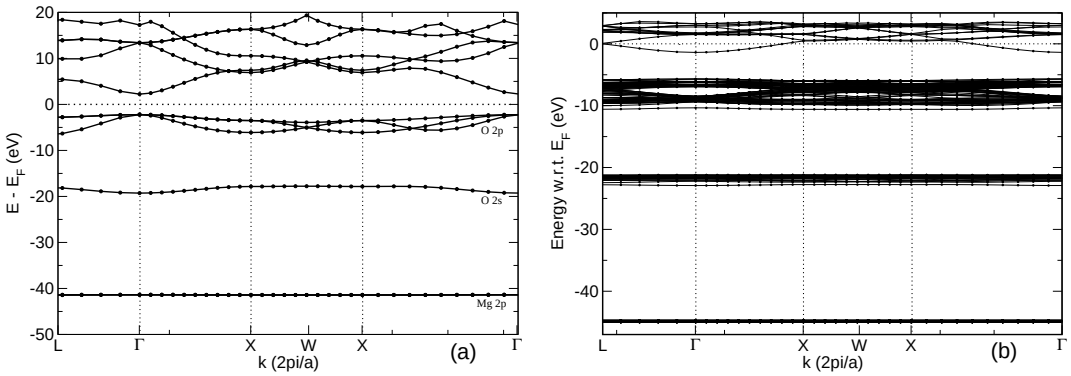

Figure 4.1: The calculated band structures of (a) pure MgO and (b) 3.7% Al-doped MgO along high-symmetry directions of the Brillouin zone. The energy is plotted with respect to the Fermi level, which is indicated by the horizontal dotted line.

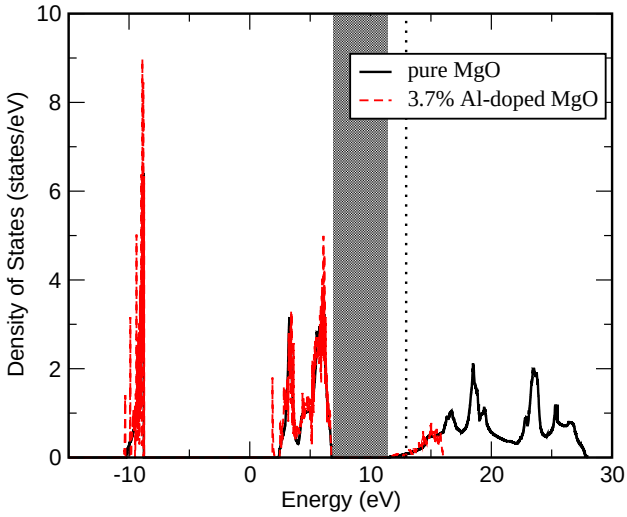

Figure 4.2: The graph shows the DOS of the pure MgO (black) and Al-doped MgO (red) system. The shaded area shows the forbidden gap of the MgO insulator, and the dotted line shows the Fermi level of the Al-doped MgO system.

4.3.2 Slab calculations on Al-doped MgO (001) surface and Mo (100) supported MgO single layer surface.

Three concentrations of Al-doped MgO, 2.78%, 1.39% and 0.69%, were studied. One Mg atom of a 3×3 cell, two Mg atoms of the 6×6 cell and one Mg atom of the 6×6 cell were replaced by Al atoms to give the respective concentrations. Four layers of MgO and a vacuum spacing of 14 Å in the [001] direction were used. The structures of the systems are shown in Fig. 4.3. As a test, the calculations on the 2.78% Al-doped MgO were carried out also allowing spin polarisation, to see if the extra electron in the system provided by the Al would create any magnetic effect. The magnetic moment of the system was found to be zero. Based upon this finding, most further calculations were performed without permitting spin polarisation. Further studies into the surface properties of the Al-doped MgO were carried out on the system with 2.78% Al dopant concentration.

The work-function of a system is computed by the following method: the Hartree Fock and bare potentials are extracted from the energy calculations, and the planar average of their sum as a function of the z direction is obtained. The calculations are done using a dipole correction in the system to rule out any dipolar interactions between the artificially created repeating cells in the [001] direction. The difference between the potential in the vacuum and the Fermi energy of the system gives the work function of the material.

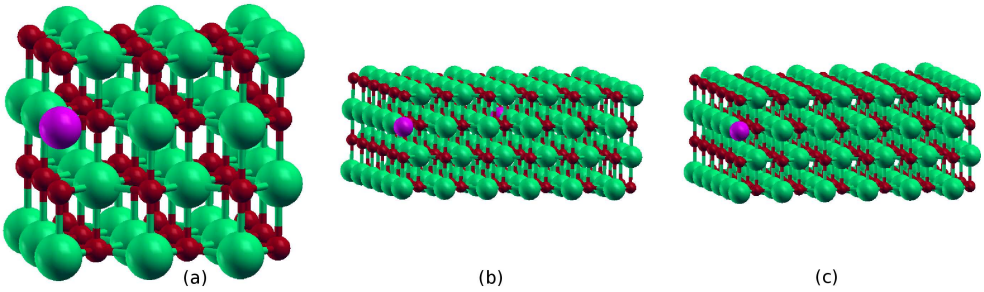

Figure 4.3: These are the structures of the cells used for calculations. Dopant concentrations of (a) 2.78%, (b) 1.39% and (c) 0.69% were used. The green, red and violet spheres represent Mg, O and Al respectively. 1 Mg atom in the 3×3 cell, 2 Mg atoms in the 6×6 and 1 Mg atom in the 6×6 were replaced by Al atoms to give the corresponding dopant concentrations.

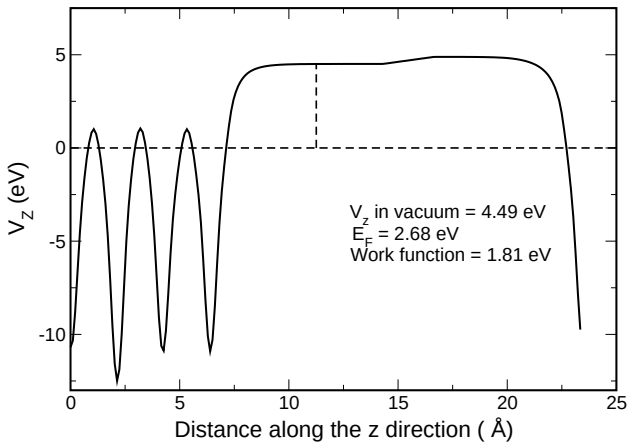

Figure 4.4: The planar average of the potential energy with respect to the distance in the z direction for the 2.78% Al-doped MgO system is shown in this figure. V_z and E_F denote the potential along z axis and the Fermi energy respectively.

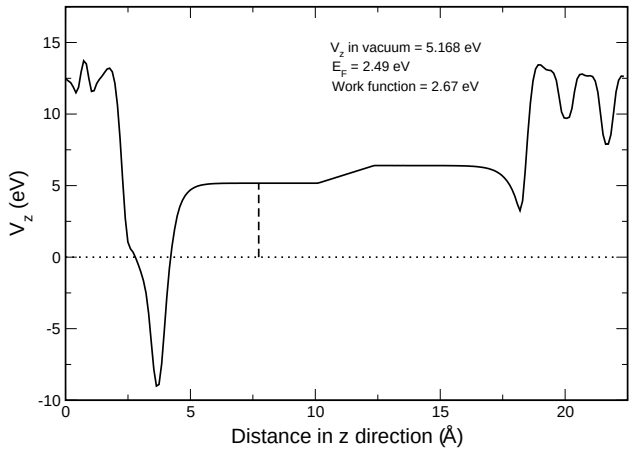

Figure 4.5: The planar average of the potential energy with respect to the distance in the z direction for a single layer of MgO over four layers of Mo is shown in the figure. V_z and E_F represent the potential in the z direction and Fermi energy respectively.

Fig. 4.4 shows the planar average of the potential energy of the 2.78% Al-doped MgO slab with respect to the distance in the [001] (z) direction. The work-function of the system was calculated to be 1.81 eV. The work-function of the slab of a single layer of MgO supported over a Mo (100) surface was also calculated and was found to be 2.67 eV. This is higher than the work-function of the Al-doped system, signifying that charge transfer from the doped substrate to the cluster is easier than the tunneling of charge from the Mo substrate through the undoped MgO to the cluster. The potential energy with respect to the distance in the z direction is shown in Fig. 4.5

The projected density of states on individual atoms was calculated for the systems of Al-doped MgO slab (Fig. 4.6) and the MgO layer over Mo slab (Fig. 4.7). In the atom-projected DOS of the Mo-supported MgO film, the position of the Fermi level in the density of states of the Mg and O atoms

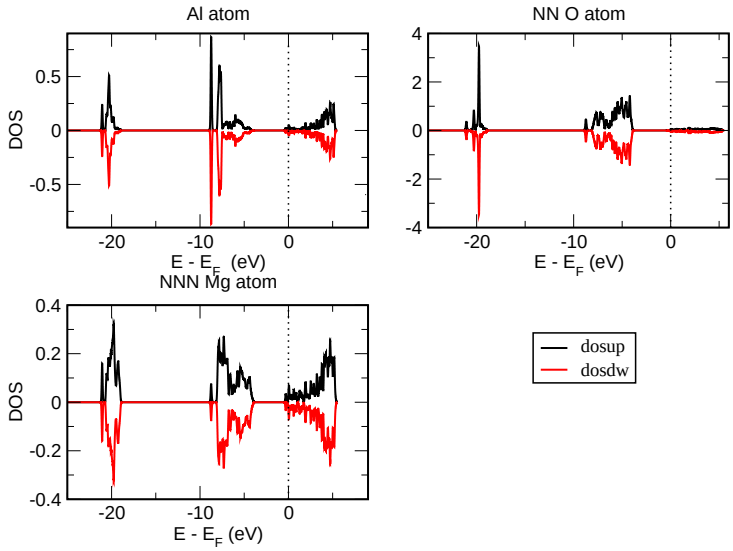

Figure 4.6: The black and red lines show respectively the up-spin and down-spin projected density of states of the 3.7% Al-doped MgO system. The projected density of states of the dopant Al atom, nearest neighbour (NN) O atom and a next nearest neighbour (NNN) Mg atom are shown. Energy is plotted with respect to the Fermi energy.

shows that they have acquired a metallic character and will allow the easy tunnelling of charges through them from the metal support to a cluster lying above. A similar observation can be made from the graph of spin-polarised projected DOS of the Al-doped MgO system. The Fermi level of the system lies in the conduction bands built out of Mg and O orbitals. The black and red lines represent the up-spin and down-spin density of states respectively. Since the system is non-magnetic the DOS of up-spin and down-spin are identical.

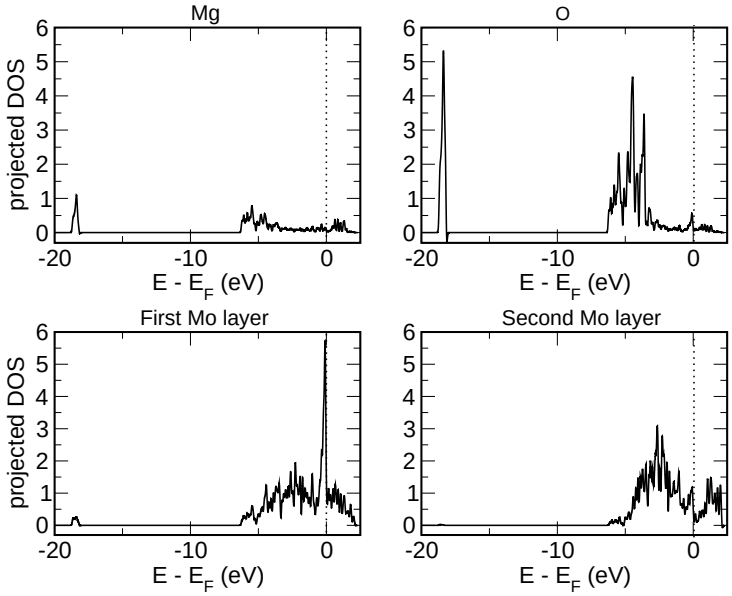

Figure 4.7: These graphs show the projected density of states on the Mg, O and Mo atoms of the first and second layer in the system MgO/Mo(001). The Fermi level of the system lies in the conduction band of the Mg and O atoms and this enables tunneling of charge through them.

4.3.3 Au cluster calculations in the gas phase

The Au_{20} clusters were considered in two geometries, the tetrahedral (T) and planar (P) geometries. Au_{20}(T) was considered in a cubic box size of 16.4 Å, and the Au_{20}(P) was considered in a tetragonal cell of dimensions 20.1 × 20.1 × 9.5 Å. The relaxed structures of the clusters are shown in Fig. 4.8. The tetrahedral geometry is favoured over the planar geometry in the gas phase by an energy difference of 1.52 eV. These calculations were done using a Makov-Payne correction which assumes the cluster to be isolated and negates any effects created due to the periodicity of the cells considered in the calculations. The tetrahedral geometry is more compact compared to the planar cluster with one atom sticking our of the closed hexagonal geometry.

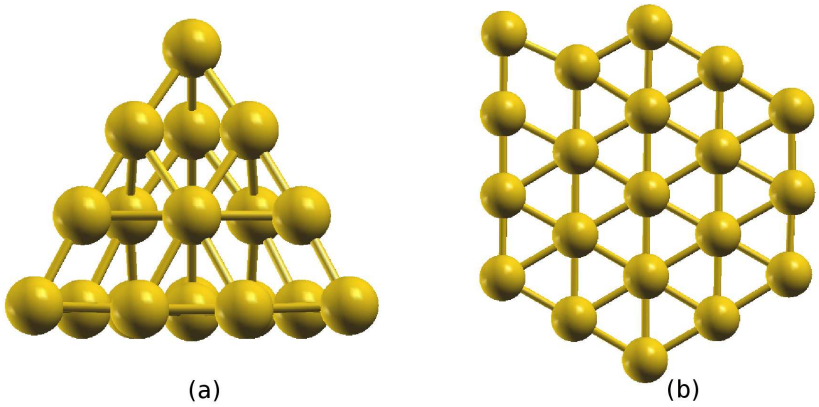

Figure 4.8: The relaxed structures of the (a) tetrahedral and (b) planar Au_{20} clusters (in vacuum) are shown in the figure.

The binding energy (BE) of the 20-atom cluster in vacuum was calculated as: BE = Energy of Au_{20}(P/T) - 20*Energy of a single isolated Au atom. It was computed to be -1.14 and 1.06 eV/atom respectively for the tetrahedral and planar geometries respectively of the Au_{20} cluster.

4.3.4 Au_{20} clusters over unsupported MgO.

In the case of Au_{20} over unsupported MgO (four layers), a 6×6 cell was considered in order to prevent the interaction between images of the Au_{20} clusters of two neighbouring cells. The Au_{20} clusters of T and P shape were placed over the slab systems and the energies of the relaxed structures in the corresponding supporting substrates were compared.

When placed on unsupported pure MgO, we found that the Au_{20} clusters preferred to adopt a tetrahedral geometry rather than a planar geometry, with an energy difference of 0.604 eV. The relaxed structures of the systems are shown in Fig. 4.9. The charge density difference at every point in the

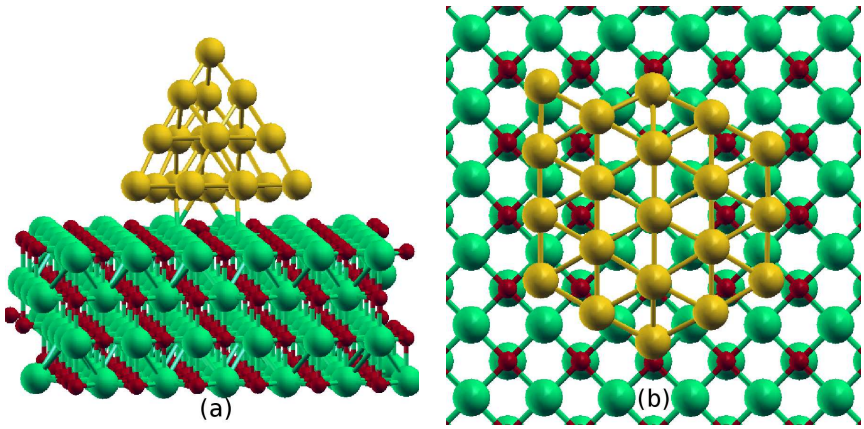

Figure 4.9: The relaxed structures of the (a) tetrahedral and (b) planar Au_{20} clusters over unsupported pure MgO are shown in the figure.

system was calculated by the relation: Charge density difference = charge density(Au_{20}/MgO) - charge density(MgO) - charge density(Au_{20}). The planar average of the charge difference for every $x-y$ plane was calculated and the integral of the charge from the point of zero charge transfer (between the Au cluster and the substrate) to the vacuum was computed. This quantity is shown in Fig 4.10. The charge transferred from the MgO substrate to the Au_{20} (T) and Au_{20} (P) were 0.596 e and 0.909 e respectively.

4.3.5 Au_{20} clusters over Al-doped MgO.

Au_{20} clusters were considered over Al-doped MgO with the Al concentration considered being 2.78%, 1.39% and 0.69%. All calculations were done using a 6×6 substrate cell. Most configurations considered consisted of the Al atom substituting a Mg atom in the second layer from the surface. A single calculation with dopant concentration 2.78%, with the Al atoms substituting Mg atoms in the third layer, was also carried out to study the effect of

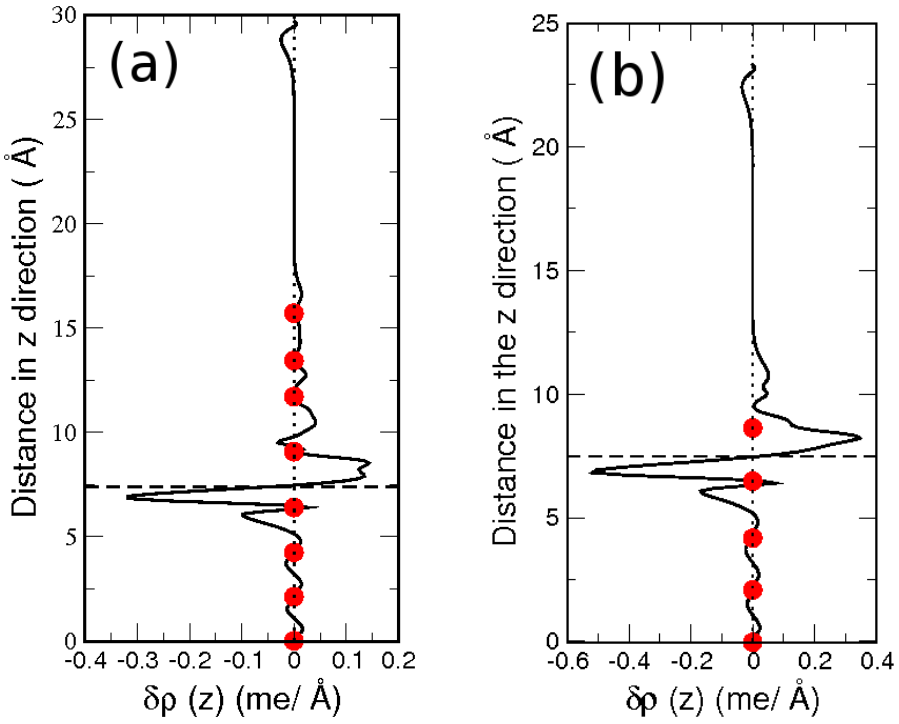

Figure 4.10: The average of the charge density difference $\delta\rho(z)$ calculated at every x-y plane for the (a) Au_{20}(T) and (b) Au_{20}(P) on MgO. The integral of the charge from the point of zero charge denisty difference between the Au cluster and the substrate (horizontal dotted line), to the vacuum give the total charge transferred from the substrate to the Au cluster. The red dots give the atomic positions along the z direction.

distance between Al and the cluster on the geometry of the Au_{20} cluster.

The binding energy is calculated according to the relation below: B.E. (P/T) = E(Au_{20}(P/T)/Al-doped MgO) - E(Au_{20}(P/T)) - E(Al-doped MgO). Here, E is the total energy of the corresponding system as computed by DFT calculations.

The binding energy of the P and T clusters on 2.78% Al-doped MgO was calculated to be -12.293 eV and -6.978 eV respectively. This can be compared to earlier results for the binding energy obtained for P and T clusters on Mo supported MgO film (-12.50 eV and -5.73 eV respectively) [57].

A graph of the energy difference between the T and P configurations with respect to dopant concentration is shown in Fig. 4.11. We find a remarkably linear relationship between the two. The higher the concentration of Al in the substrate, the higher is the energy difference between the P and T clusters over the doped substrates. The least concentration of Al required to favour the planar geometry over the tetrahedral geometry is 0.38%. The energy difference between the tetrahedral and planar clusters is found to increase slightly in magnitude from -3.796 to -3.862 eV when the Al is moved from the second layer to the third layer. On Mo-supported MgO [57], the energy difference between the P and T clusters over the substrate was found to be -3.3 eV. The more negative the energy difference the more stable the planar geometry is with respect to the T geometry, and the P geometry is found to be more favoured over the T geometry when it is placed on Al-doped MgO than on Mo-supported MgO.

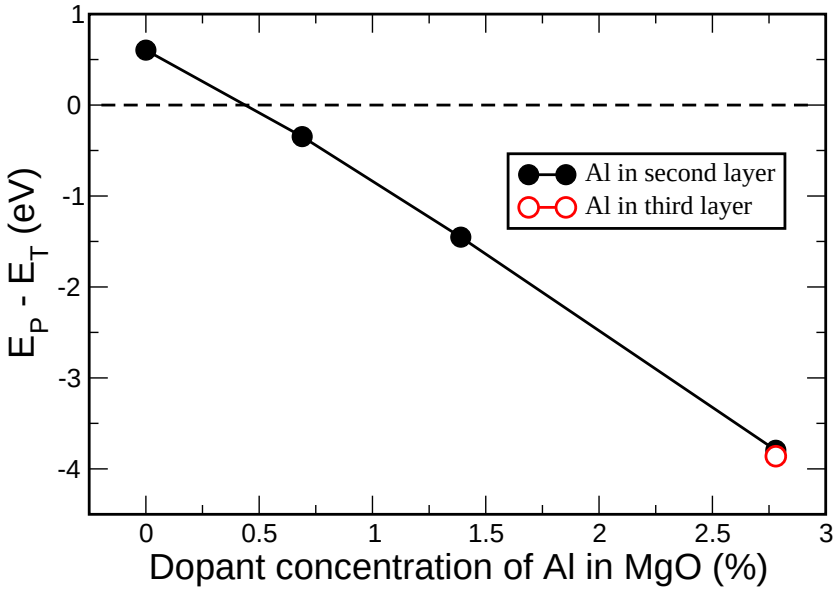

Figure 4.11: The linear relation between the dopant concentration of Al in MgO and the stability of the planar geometry over the tetrahedral structure is shown in this graph. The Mg atoms in the second layer from the surface were replaced by Al atoms to give these dopant concentrations.

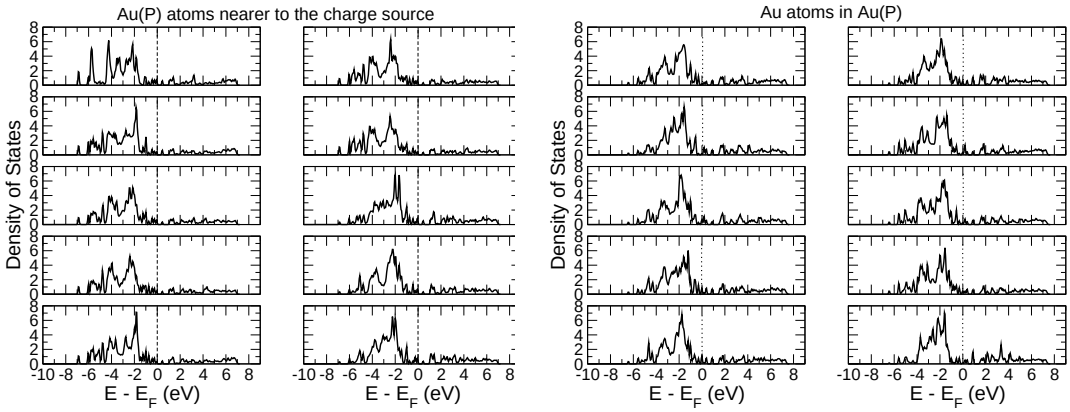

Figure 4.12: The projected density of states of the Au atoms of the P structure are shown above.

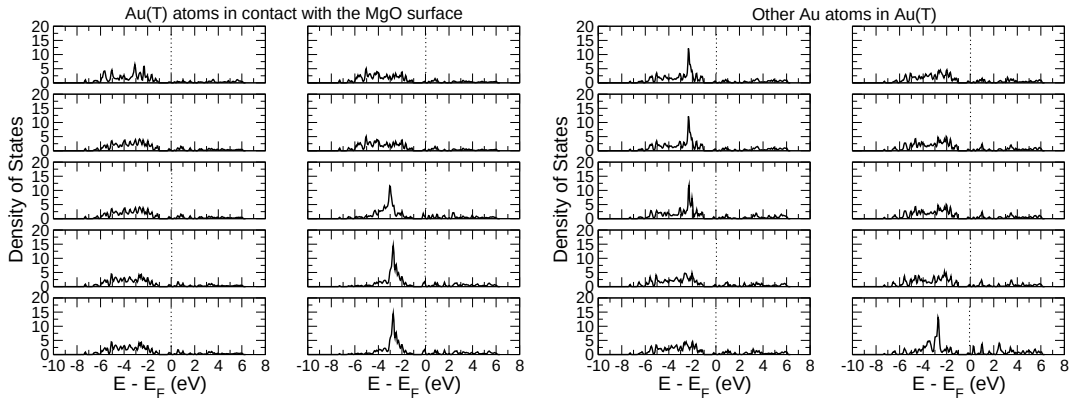

Figure 4.13: The projected density of states of the Au atoms in the T structure are shown.

Choosing a particular case, further analysis was done with the 2.78% Al-doped MgO system. The projected density of states for this system was calculated. The density of states of the 20 individual Au atoms can be seen in Figs. 4.12 and 4.13.

We also examined the charge density of these systems. The charge density difference between the Au cluster on the doped substrate and the Au cluster alone and doped substrate alone were calculated. The charge transfer between the 2.78% Al-doped MgO substrate and the cluster is plotted in Fig. 4.14. The isosurfaces of 0.0025 e/Å^3 for the T cluster and 0.0013 e/Å^3 for the P cluster are shown. The isosurface plot of the charge transfer for the P cluster system clearly shows an accumulation of charge at the interface of the cluster and the substrate. A planar average of the charge density difference in the x-y plane with respect to the z direction is shown in Fig. 4.14. The charge transferred was calculated by integrating the plot from the region where the graph cuts the y-axis (point of zero charge transfer between the

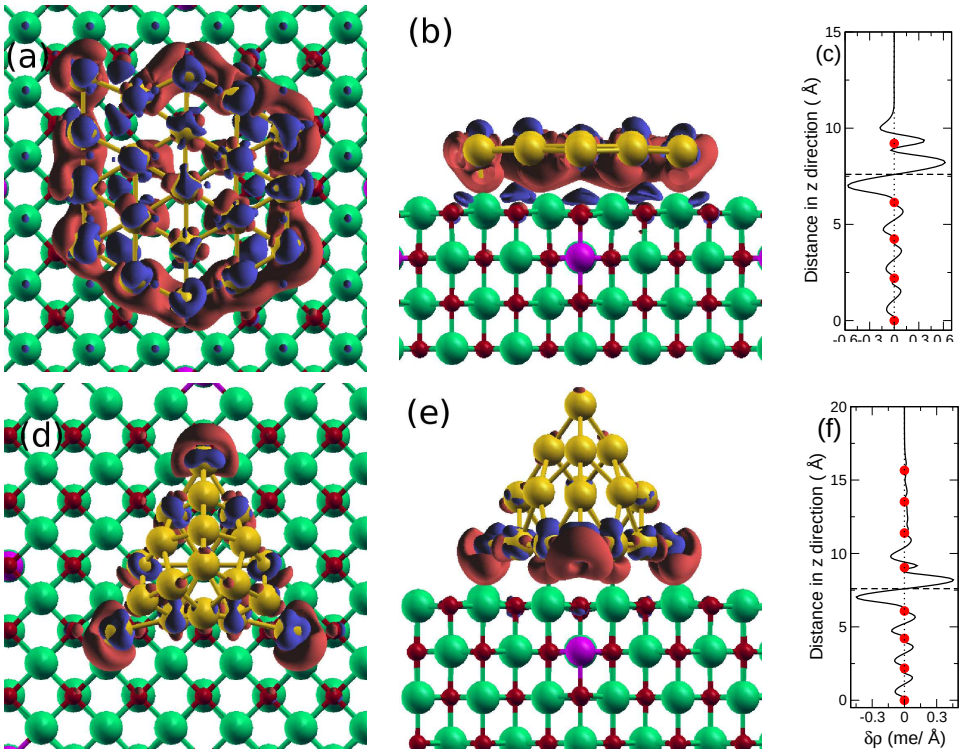

Figure 4.14: The isosurface plots for the values 0.0025 e/$\AA^3$ and 0.0013 e/$\AA^3$ are shown for the Au_{20} clusters (P/T) over 2.78% Al-doped MgO. The green, red, violet and yellow colour atoms represent Mg, O, Al and Au respectively. The blue and pink isosurfaces show the regions of charge depletion and charge accumulation respectively. The isosurface plot of the (a) Au_{20}(P)/Al-doped MgO top view, (b) side view and (c) a graph of the planar average of the charge difference along the z direction can be seen. The bottom row shows the isosurface plot of (d) Au_{20}(T)/Al-doped MgO top view, (e) side view and (f) a graph of the planar average of the charge difference along the z direction. Note the excess electronic charge distribution for the planar Au_{20} cluster located at the interface between the cluster and the substrate.

cluster and the substrate) to the vacuum. The values calculated for the T and P supported clusters are 0.89 e and 1.12 e respectively. When the Al atom was placed in the third layer, the charge transfer was found to increase to 1.096 and 1.305 e respectively for the T and P clusters. In Mo-supported MgO [57], the reported charge transfer to the T and P clusters are 1.06 and 1.62 e respectively.

4.4 Summary

The Au_{20} clusters are found to prefer a flat geometry when doping promotes an increased charge transfer from the substrate to the Au cluster. We have achieved this results by a simple method of doping the substrate MgO with Al. The substitution of Mg with Al atoms creates a delocalization of an extra electron (per Al atom) in the substrate which enables a strong charge transfer towards the Au cluster. The positively charged Al ions in the substrate also help lower the energy of the P cluster by the electrostatic energy between them.

A linear relation between the concentration of the dopant in MgO and the energy difference between the T and P geometries was observed. It shows that we can control the geometry and the stability of the geometry of the Au_{20} clusters quite effectively by just manipulating the dopant concentration in the substrate. Earlier methods of placing Au clusters over metal supported MgO [57] and application of electric field [54] give similar results though the preparation of the thin films of MgO over Mo or Ag may be difficult in the laboratory and the electric field suggested in the earlier calculations (1 V/nm)

is impracticably high. In the method involving MgO/Mo, the stability of the planar cluster over the tetrahedral cluster is controlled by the number of MgO layers. The lesser the number of layers, the greater will be the stability of the planar cluster. These experiments are very hard to do. Even if they are successful experimentally, applying these techniques in practical realizations is tedious. The metal support can make the system difficult to transport and the application of electric field will be difficult. We have suggested an approach which promises to be much simpler experimentally. The energy barrier between the two cluster geometries can be controlled by just the concentration of the dopant in the substrate. The system consists of doped MgO which is light and very convenient to carry and transport.

Chapter 5

Conclusions

In the first portion of the thesis we have investigated the miscibility of metals over the W(110) surface. We have performed *ab initio* calculations on fifteen combinations of metals involving a magnetic and a non-magnetic metal co-deposited on W(110) substrate. Except for alloys with Ag, all other surface alloys were stable. We found that even bulk-immiscible pairs of metals form stable alloys over the surface of W(110). We have tried to analyse the factors governing the energetics of these strain-stabilized surface alloys.

Alloys of Fe and Co were found to be magnetic in nature unlike the alloys of Ni. Most alloys of Fe, except for $Fe_{0.25}Pb_{0.75}$/W(110), were found to show an enhanced magnetic moment with respect to the bulk magnetic moment of Fe. In agreement with previous authors [34], the magnetic moment of the monolayer of Fe/W(110) was found to be enhanced by around 17% in comparision to its bulk magnetic moment of 2.2 μ_B. In contrast to alloys of Fe, all alloys of Co seem to show a lower magnetic moment per Co atom than the bulk magnetic moment of Co which is 1.7 μ_B. W is found to interact

anti-ferromagnetically with the magnetic atoms on the overlayer.

We find that the stability of the surface alloys do not follow a simple size dependent rule that the mean atomic sizes of the atoms of the alloy should be close to the substrate lattice spacing. This is due to the presence of chemical interactions in addition to the elastic interactions between the atoms of different sizes forming the alloy. Even in cases where the elactic interaction may favour surface alloy formation, the chemical interaction can be large enough to disfavour atomic level mixing of the atoms. The elastic energies of the phase-segregated monolayers on the substrate also need to be considered to analyse the stability of the strain-stabilized surface alloys. Due to these three factors, it is difficult to formulate a single and simple rule to dictate the stability of such alloys. An analogy to the first Hume-Rothery rule for bulk alloys may not be possible for surface alloys.

The effective atomic sizes of the metals on the W substrate were also computed. They were found to be different from the bulk; in the magnetic atoms, they were found to be larger than the bulk size, and in case of the non-magnetic atoms, the preferred sizes were found to be smaller than their bulk sizes. Of all the alloys considered, Fe-Au, Co-Cd, Ni-Au, Ni-Cd and Ni-Pt may be promising candidates that may be realizable experimentally. Both chemical and elastic interactions favour the formation of these alloys.

As a future project, we wish to try to explain the factors determining the surface sizes of the atoms on the W(110). We have considered only a small 2×2 surface unit cell in our calculations. We can do calculations on larger unit cells and see if we can try to observe any trend favouring any particular pattern over others and study the factors deciding them.

In the second half of the thesis, we have probed the ability to control and tune the morphology of a 20-atom Au nanocluster. For this purpose, we have compared the energetics and stability of two forms of the cluster, the planar (P) and the tetrahedral (T) geometry in vacuum, on pure MgO substrate, and supported on Al-doped MgO.

Negatively charged Au clusters were found, by earlier authors, to be more catalytically active, especially in oxidation reactions [56]. On adsorption of an oxygen molecule on the Au cluster, the O-O bond gets activated due to the occupation of electrons in the antibonding orbital of the oxygen molecule [55]. It was found that a planar Au cluster absorbs more charge from the substrate than the tetrahedral cluster and hence it can be believed that the planar Au cluster is more catalytically active than the tetrahedral cluster. Previous authors have found that the geometry of the cluster can be altered from the stable, higher symmetry tetrahedral structure to the planar, lower symmetry structure by using: (1) metal-supported thin films of MgO as the substrate [57], or (2) applying an electric field to a metal supported thick film of MgO [54]. We have attempted to produce the same result of these techniques by a relatively simpler method: by the doping the substrate.

The preparation of thin films (less than seven layers) of MgO over Mo or Ag can be very tedious and the electric field required (1 V/nm) to produce the change in dimensionality of the cluster on these systems are impracticably high. We wish to suggest the method of doping the substrate to experimentalists as a simpler method to control the geometry of a Au_{20} nanocluster. The dopant atoms in the substrate may also act as an anchor site, and prevent diffusion of the Au clusters over the surface. These properties can be

very useful considering the catalytic property of Au nanoclusters. The planar cluster has more surface area than the tetrahedral cluster and it is found to have more sites of high charge accumulation, than the tetrahedral cluster. These sites may be the active sites for various reactant molecules to adsorb.

We also found that the energy difference between the planar and tetrahedral geometry has a linear relation to the dopant concentration. The higher is the dopant concentration, the more stable is the planar geometry, with the energy difference increasing in magnitude. The energy difference was found to increase slightly when the dopant Al atom was shifted from the second to the third layer from the surface. The electrostatic attraction between the Al charge source and Au (negative) cluster stabilizes the cluster's planar geometry over the substrate.

For future projects, we can try to adsorb oxygen molecules onto the Au_{20} clusters and study the activation of the O-O bond in our system. We also wish to try other sizes of Au clusters and see if we can observe similar results for bigger clusters. We would also like to find out if the method of doping can be a general technique to initiate charge transfer to a supported cluster and creating a structural change in the cluster.

Bibliography

[1] Hertel, I. V., ed. (1991) Z. Phys. D. At. Mol. Clusters **19**.

[2] Hertel, I. V., ed. (1991) Z. Phys. D. At. Mol. Clusters **20**.

[3] P. Hohenberg, W. Kohn, Phys. Rev. **136** (1964) 864B.

[4] W. Kohn, L. J. Sham, Phys. Rev. **140** (1965) 1133.

[5] http://www.pwscf.org/

[6] M. Born and J.R. Oppenheimer. Zur Quantentheorie der Molekeln. Annalen der Physik **84**, 457-484, 1927.

[7] C. Eckart. Phys. Rev. **46**, 383-387, 1934.

[8] P. Hohenberg and W. Kohn, Phys. Rev. **136**, B864 (1964).

[9] R. O. Jones and O. Gunnarsson, Rev. Mod. Phys. **61**, 689 (1989).

[10] J. P. Perdew and Y. Wang, Phys. Rev. B **46**, 12947 (1992).

[11] A. D. Becke, J. Chem. Phys. **38**, 3098 (1988).

[12] J. P. Perdew, K. Burke, and M. Ernzerhof, Phys. Rev. Lett. **77**, 3865 (1996).

[13] J. P. Perdew, K. Burke, and M. Ernzerhof, Phys. Rev. Lett. (E) **78**, 1396 (1997).

[14] J. C. Phillips, Phys. Rev. **112**, 685 (1958).

[15] J. C. Phillips and L. Kleinman, Phys. Rev. **116**, 287 (1959).

[16] M. L. Cohen and V. Heine, Solid State Physics **24**, 37 (1970).

[17] G. B. Bachelet, D. R. Hamann, and M. Schluter, Phys. Rev. B **26**, 4199 (1982).

[18] D. Vanderbilt, Phys. Rev. B. 41, 8412 (1990).

[19] H. J. Monkhorst and J. D. Pack, Phys. Rev. B **13**, 5188 (1976).

[20] C. L. Fu and K. M. Ho, Phys. Rev. B **28**, 5480 (1983).

[21] M. Methfessel and A. T. Paxton, Phys. Rev. B **40**, 3616 (1989).

[22] N. Marzari, D. Vanderbilt, A. D. Vita and M.C. Payne, Phys. Rev. Lett. **82**, 3296,(1999)

[23] R. P. Feynman Phys. Rev. **56**, 340, (1939).

[24] O.H. Nielsen and R.M. Martin Phys. Rev. Lett. **50**, 697, (1983).

[25] O.H. Nielsen and R.M. Martin Phys. Rev. B **32**, 3780, (1985).

[26] O.H. Nielsen and R.M. Martin Phys. Rev. B **32**, 3792, (1985).

[27] W. Hume-Rothery and H. M. Powell, Z. Krist. **91**, 13 (1935)

[28] Thayer G E, Ozolins V, Schmid A K, Bartelt N C, Asta M, Hoyt J J, Chiang S and Hwang R Q Phys. Rev. Lett. **83** (2001) 1379

[29] L. Nielsen, F. Besenbacher, I. Stensgaard, E. Lægsgaard, C. Engdahl, P. Stoltze, K. W. Jacobsen, and J. K. Nørskov, Phy. Rev. Lett. **71**, 754 (1993).

[30] H. Röder, R. Schuster, H. Brune and K. Kern, Phys. Rev. Lett. **71**, 2086 (1993).

[31] J, Honolka, T. Y. Lee, K. Kuhnke, A. Enders, R. Skomski, S. Bornemann, S. Mankovsky, J. Minar, J. Staunton, H. Ebert, M. Hessler, K. Fauth, G. Schütz, A. Buchsbaum, M. Schmid, P. Varga and K. Kern, Phys. Rev. Lett. **102**, 067207 (2009).

[32] A. Ney, P. Poulopoulos and K. Baberschke, Europhys. Lett., **54** (6), pp. 820825 (2001).

[33] M. C. Muñoz, L. Chico, M. P. López-Sancho, J. I Beltrán, S Gallego and J Cerdá, Journal of Physics: Conference Series **30** (2006) 215223.

[34] T. Andersen and W. Hübner, Phys. Rev. B **74**, 184415 (2006).

[35] N. W. Ashcroft and N. D. Mermin, *Solid State Physics* (Thomson Asia Pte. Ltd, Bangalore, 2004).

[36] M. Marathe, M. Imam, S. Narasimhan, Phys. Rev. B **79** (2009) 085413.

[37] M. Imam, M. Marathe, S. Narasimhan, J. Chem. Sci., Vol. 120, No, (2008) 621.

[38] M. Marathe, M. Imam, S. Narasimhan, App. Surf. Sci. **256** (2009) 449.

[39] D. Sander, A. Enders and J. Kirschner, Europhys. Lett. **45** (2), pp. 208-214 (1999).

[40] E. C. Stoner, Proc. R. Soc. London Ser. A **169** (1939) 339.

[41] E. Cordwell, D. Hull, Phil. Mag. **19** (1969) 951.

[42] B.Hammer, J. K. Norskov, Nature **376** (1995) 238.

[43] W. Schmidbaur, W. Gordon, Chem. Zentralbi, **106** (1935), 514.

[44] M. Haruta, T. Kobayashi, H. Sano and N. Yamada, Chem. Lett. **4** (1987) 405.

[45] Hironori Tsunoyama and Tatsuya Tsukuda, J. Am. Chem. Soc. (2009), **131**, 1821618217.

[46] Knight, W. D. Clemenger, K. de Heer, W. A. Saunders, W. A. Chou, M. Y. Cohen, M. L. Phys. ReV. Lett. (1984), **52**, 2141.

[47] A. Sanchez, A. Abbet, U. Heiz, W. D. Schneider, H. Hakkinen, R. N. Barnett, Uzi Landman, J. Phys. Chem. A, **103** (1999) No. 48

[48] J. Li, Xi Li, H. Zhai, L. Wang, Science **299** (2003)

[49] H.-G. Boyen et al, Science **297** (2002) 5586, 1533-1536.

[50] R.Elghanian, J.J. Storhoff, R.C Mucic, R. L. Letsinget, C. A. Mirkin, Science **277** (1997) 1078.

[51] Melanie Homberger and Ulrich Simon, Phil. Trans. R. Soc. A **vol. 368 no. 1915** (2010) 1405-1453.

[52] D. Ricci, G. Pacchioni, U. Landman, Phys. Rev. Lett. **97**, (2006), 036106.

[53] C. Zhang, B. Yoon, U. Landman, J. Am. Chem. Soc. (2007), **129**, 2228.

[54] B. Yoon, U Landman, PRL **100** (2008) 056102.

[55] L.M. Molina and B. Hammer, Journal or Catalysis **233** Issue 2 (2005) 399-404.

[56] Chiang Sun, Puru Jena, Yound Dok Kim, Matthias Fischer and Gerd Gantefor, Journal of Chemical Physics **120** (2004) 6510.

[57] C. Harding, V. Habibpour, S. Kunz, A. Farnbacher, U. Heiz, B. Yoon, U. Landman, J. Am. Chem. Soc. **131** (2009) 538.

[58] J. P. Perdew, J. A. Chevary, S. H. Vosko, K. A. Jackson, M. R. Pederson, D. J. Singh, and C. Fiolhais, Phys. Rev. B **46**, (1992) 6672; **48** (1993) 4978.

[59] G. Makov and M. C. Payne, Phy. Rev. B. Vol **51**, Number 7 (1995).

[60] L. Bengtsson, Phys. Rev. B, Vol **59**, Number 19 (1999).